European Gravitational Observatory

Internship report

Magnetic noise in Avanced Virgo Plus : the case study of Faraday isolators

Jean-Loup RAYMOND

2022

Abstract

Gravitational waves observatories rely on interferometry to detect the variations of space-time curvature corresponding to these waves. These varitions require very sensitive instrumentation to be identified reliably and studied in detail. As a result, the interferometer is potentially sensitive to noises, and the knowledge of the environmental sources of noise as well as how they couple to the measurements is essential to produce exploitable data.

In particular, due to the presence of numerous ferromagnetic and conductive materials on the different optical benches and structures of the interferometer, it is important to characterize and study how environmental magnetic fields couple to and eventually influence the interferometer. In this study, we focus on the simulation of a bench, a critical place for magnetic coupling due to the presence of a Faraday Isolator, an optic component that uses an intense static magnetic field. Then, we present the construction of a magnetic shield for that component in order to reduce its influence.

We model the suspended injection bench of Virgo based on executive drawings of that bench. The model is refined to implement a possible experimental setup of injection of a magnetic field to measure the coupling. This experiment is then realized and the results are confronted with simulation. Lastly, the process of elaborating a magnetic shield around the Faraday Isolator in a very constrained volume is detailed, and a mitigation factor is obtained. A specific source of environmental noise is also studied and will be commented in appendice.

Acknowledgements

First and foremost, I would like to thank Irene Fiori for her excellent guidance along my internship, her trust and help in my first experience in Italy and her friendliness.

I would also like to thank the entire Virgo environmental noise team, with whom I have spent very nice moments, for their help, warm welcome and wise advices.

I would also like to thank Andrea Chincarini for his friendliness and expert advice on simulation and studies of magnetic fields during the internship.

Lastly, I would like to thank François Chevoir and Anaël Lemaître for their careful review of my work as my academic tutors for this internship.

Contents

Introduction

The aim of the Virgo interferometer is the observation of gravitational waves.

The gravitational waves, predicted by the general relativity, are oscillations of the curvature of spacetime generated by accelerated bodies. These waves are polarized, propagate at the speed of light, and their intensity diminishes inversely proportionally with the distance from the source. For instance, a gravitational wave modifies the distance between two free falling masses as it progresses through the space between them. This condition is realized by suspending the masses. This modification, relative to the distance between the masses, is extremely small (of the order of 10^{-21}). Thus, to observe the furthest objects, a higher sensitivity is needed. An example of gravitational wave source is the coalescence of two high density bodies, for instance two black holes gravitating around each other. Gravitational waves from pairs of coalescing black holes and neutron stars have been observed by current gravitational waves observatories [9].

These detectors rely on the principles of interferometry to detect gravitational waves. A laser beam is emitted, splitted in two orthogonal beams that go in perpendicular arms, are reflected within these arms and converge back to the beam splitter. Then, the phase shift between the overlapped beams exiting the detector is detected via a photodiode. When a gravitational waves comes across, the spacetime curvature creates a difference of length in the two arms, hence a difference in time needed to travel along the arms for the two beams. It is from that difference I would introduce later, in Chapter 1, that the information on the gravitational waves is extracted.

The present gravitational waves observatories, including Virgo, are ground-based detectors. Albeit an advantage for the feasability and realisation of the interferometer, this also exposes it to a vast number of environmental noises in addition to the instrumental noises. As a result, these detector are able to detect gravitational waves with sufficient reliability only in a determined range of frequencies - from $10Hz$ to $10kHz$. In particular, the low frequencies are especially perturbated, due to the superposition of various noises - see sensitivity curve, figure 3 -, among these noises is the effect of the environmental magnetic field.

Magnetic fields are created typically by infrastructures of the experiment (e.g. electrical motors of the pumps, stray fields from power supply, etc...). They can affect the interferometer in different ways, by moving benches directly by electromagnetic force for instance. This results in parasitic movements of the benches that make the interferometer blind to certain frequencies.

In order to reduce magnetic noise influence on the interferometer, one has to identify and mitigate the sources of the noise or reduce the coupling of the noise to the interferometer. An example of noise source identification mitigation is that of the magnetic noise created but natural gas pipes around the Virgo site, such a study is presented in the Appendix. One also has to identify the most critical components in the interferometer and reduce the coupling. The study presented here describes the simulation of such a coupling, as well as an experimental way to measure it. It also deals with the third and last aspect that is the shielding of sensitive components to mitigate the coupling.

Chapter 1 starts by presenting the Virgo interferometer, the principles of the detection and the effect of noises. In chapter 2, we present a focus on a sensitive optical component, a Faraday

isolator. Then, in chapter 3, the measurements and modelling on that component are developped. The fourth chapter is dedicated to the suspended injection bench, and the choices made for its simulation. In chapter 5, the results of the simulation are discussed. Chapter 6 is dedicated to the sensor used to detect the effect of the magnetic field on the bench. Chapter 7 focuses on the experimental topics of the coupling measurement. Chapter 8 presents generalities on magnetic shielding and the mitigation of magnetic noise. Chapter 9 shows the steps of elaborating a shield for a Faraday Isolator on suspended detection bench. Lastly, chapter 10 details the preparation for the next steps and future improvements to the study. The appendix describes the process of locating the source of a magnetic noise seen in Virgo.

1 Noise effects and interferometer sensitivity

General relativity predicts that accelerated bodies emit gravitational waves, variations of the curvature of spacetime that propagate at the speed of light. These waves are polarized orthogonally to the direction of propagation - two states are possible, called $+$ and $\times$ -, and were first detected in 2015 by LIGO and Virgo, three ground-based gravitational waves detector. This study focuses on the Virgo interferometer, and the study of solutions to be implemented for the next phase, the Advanced Virgo 5^{th} observation run (O5).

1.1 Detection principles and sensitivity

The Virgo interferometer is a Michelson laser interferometer with resonant optical cavities in the arms and double power recycling. An infrared laser beam ($\lambda = 1064nm$) goes through an input mode cleaner, a 140m suspended optical cavity which allows only the main laser frequency and fundamental laser mode to resonate and proceed allowing only certain frequencies to proceed and enter the interferometer. The beam then goes through a Faraday Isolator, to the beam splitter (BS) mirror. This separates the beam in two orthogonal beams entering each one of the arms, named North and West. Each arm is 3 km long and consists of a Fabry-Pérot cavity. The light travels the arm on average 300 times before converging back to the beam splitter.

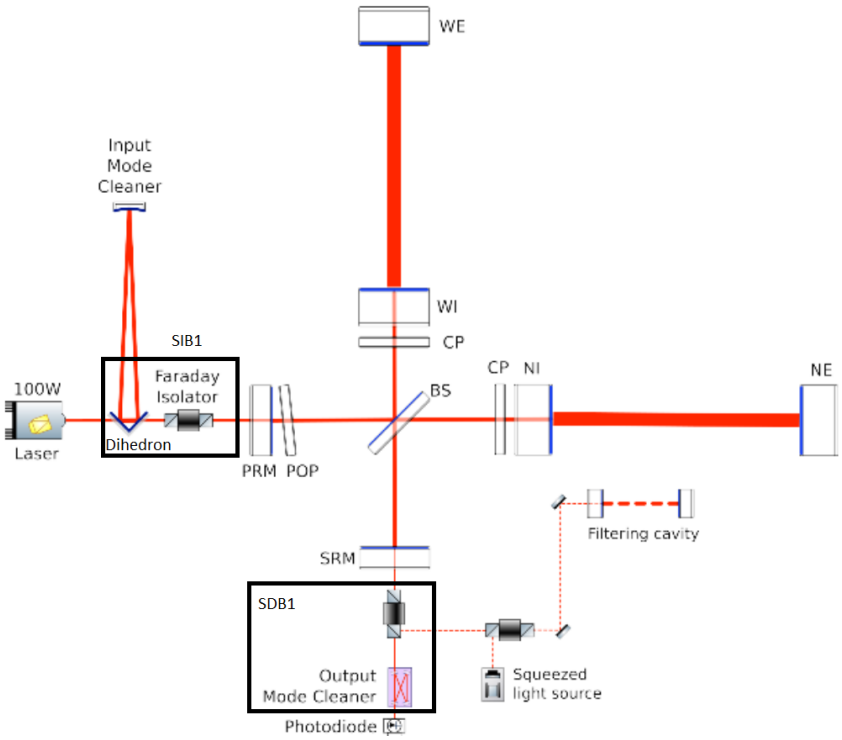

Figure 2: Advanced Virgo plus (AdV+) interferometer simplified scheme [6]

From the beam splitter the light is partially reflected back towards the laser, and partially goes along the detection part. A power recycying mirror (PRM) intercepts and reflects back towards the interferometer the light that from the BS follows the path back towards the laser. Along the detection path, a signal recycling mirror (SRM) has the same function. Through this SRM, the beams from the arms superpose to form an interference pattern which, after passing a Faraday isolator, is measured by a photodiode. On the output port, squeezed vacuum states are injected to reduce quantum noise, by either reducing the amplitude (reducing radiation pressure) or the

phase fluctuations (reducing shot noise) at the expense of the other. To reduce the phase noise due to the presence of air, the trajectory of the beams is immersed in a vacuum chamber inside of which the air pressure is 10^{-9}mbar.

When a gravitational waves impinges the detector, the differential length of the arms changes slightly by a δL. This variation is described by :

$$\frac{\delta L}{L} = C \times h \tag{1}$$

Where $0 \leqslant C \leqslant 1$ is a geometric factor allowing to take into account the direction of the incoming wave and its polarization, h is the amplitude of the wave, and L is the optical length of the arm. When no gravitational waves impinges the detector, the length of the arms is ajusted to realize a disruptive interference on the photodiode. The variation of optical length of the arms results in a difference of power received by the photodiode.

Typically, the frequency spectrum of the calibrated photodiode signal is produced. This is the quantity shown in Figure 3. [1]

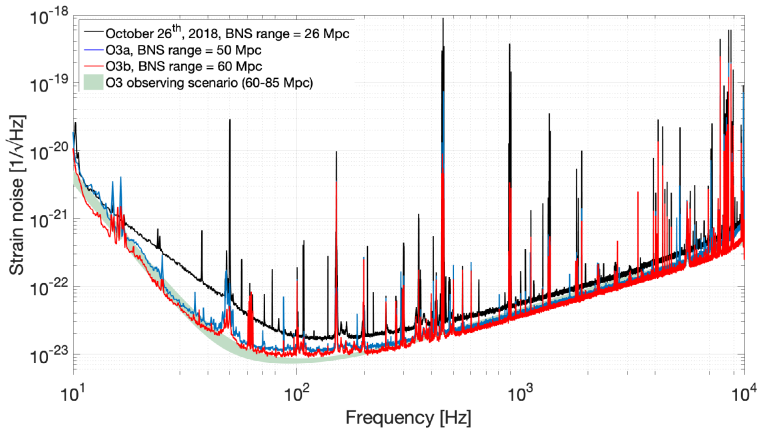

Figure 3: Virgo sensitivity measured in 3^{rd} observation run [4]

In the absence of a GW signal this quantity measures the intrinsic noise of the interferometer.

[1] In particular, Power Spectral Density (PSD) and its square root will be used in the following. The PSD of a variable x of Fourier transform $\hat{x}$ is approximated, for a finite period of time T, by

$$PSD_T(f) = \frac{|\hat{x}_T(f)|^2}{T}$$

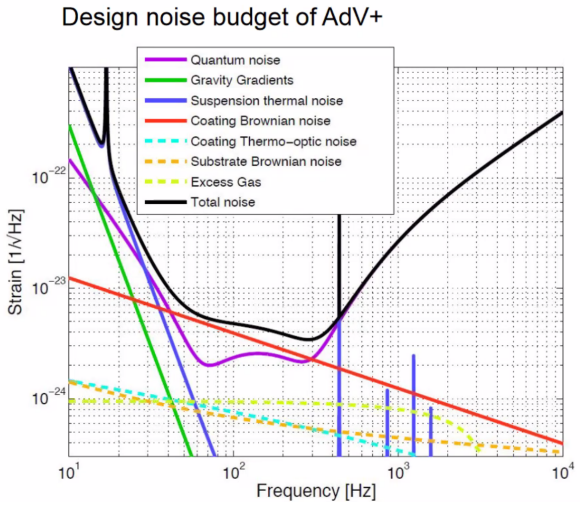

Figure 4: Design sensitivity curve (black line) of the Advanced Virgo + detector. Colored lines correspond to the estimated noise contributing to the sensitivity [3]

The contribution of every noise observable can also be quantified by modelling its effect on the sensitivity as shown in figure 4, an the quadratic sum of all noises is referred to as sensitivity curve. This determines the performance of the interferometer in detecting gravitational waves for a band of frequencies.

1.2 Noises and coupling mechanisms

The different noises can limit the sensitivity at certain frequencies. In that case, reducing their impact has a direct influence on interferometer sensitivity. This study will focus on the influence of the magnetic noise, and how to mitigate it.

The most direct noise is seismic noise. A mechanical excitation of a part of the interferometer can have various consequences depending on where this is located. The geometry of the interferometer might be affected, ultimately modifying the light power received by the photodiode. For instance, the following disturbances can happen due to seismic noise :

- Misalignment of the optical instruments due to a translation
- Misalignment of the optical instruments due to a rotation
- Non-null DARM due to a longitudinal translation of a mirror
- Non-null DARM due to the rotation of a mirror

To avoid these perturbations, the benches and mirrors are suspended inside of the vacuum chambers (called towers). This suspension system filters ground vibrations with frequency above a few Hz, mitigating noise in the range of frequencies of the most common seismic disturbances.

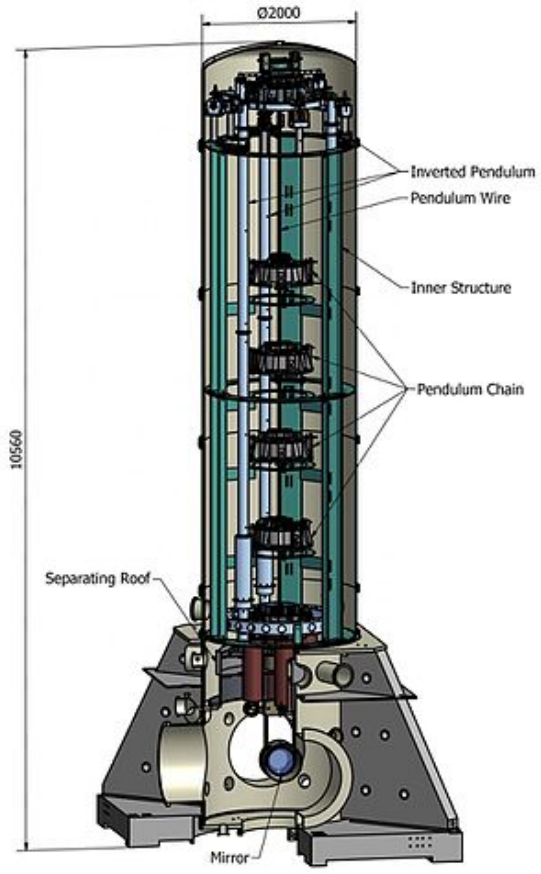

Figure 5: Virgo mirror suspension drawing [1]

In addition to displacements due to ground seismic noise, other noise sources can produce a displacement of the test masses or other optical components, particularly the magnetic noise. These couplings can have different origin.

The first type of coupling occurs in the presence of permanent magnets on the benches, for example in the magnet-coil actuators used to position the bench, or in optical components like the Faraday isolator, as discussed later. For an elementary volume of magnetization $\overrightarrow{m}$ immersed in a magnetic field $\overrightarrow{B}$, the expression of elementary potential energy E and elementary force and torque excerted on the volume are, respectively :

$$E = -\overrightarrow{m}.\overrightarrow{B} \tag{2}$$

$$\overrightarrow{f} = -\overrightarrow{\nabla}(\overrightarrow{m}.\overrightarrow{B}) \tag{3}$$

$$\overrightarrow{t} = -\overrightarrow{m} \times \overrightarrow{B} \tag{4}$$

By integrating these equations on the ferromagnetic volume, we obtain forces and torques that act on the bench directly.

Another type of coupling possible is due to Eddy currents on conductive surfaces (see figure 13). The time derivative of the magnetic flux through this surface induces an electromotive force $EMF = \frac{-d\phi}{dt}$ creating currents on the surface.

These currents create a magnetic field opposed to the initial field and locally distorting the magnetic field. In particular, if the magnetic field flux changes in time because of a non-stationary magnetic field, the induced magnetic field will increase with the frequency of the field. This results

in a low pass filter, with a higher slope for higher conductivity materials. The conductive surfaces are also subject to Lorentz force because these currents are moving charged particles in a magnetic field :

$$\overrightarrow{F} = q\overrightarrow{v} \times \overrightarrow{B} \tag{5}$$

These mechanical effects can take place in all conductive surfaces of the tower, the suspension, and the bench. The effect of these contributions will be quantified and compared in the rest of this study.

1.3 Magnetic coupling locations

There are different types of sensitive locations.

- The mirrors of the Fabry-Perot cavities, for instance, are particularly critical for the interferometer. These mirrors are suspended, and controlled using tiny magnets (2.5mm diameter, 1T) glued directly onto the mirror back face.
- Permanent magnets used in optical components, notably Faraday Isolators

These places are presented in figure 6 :

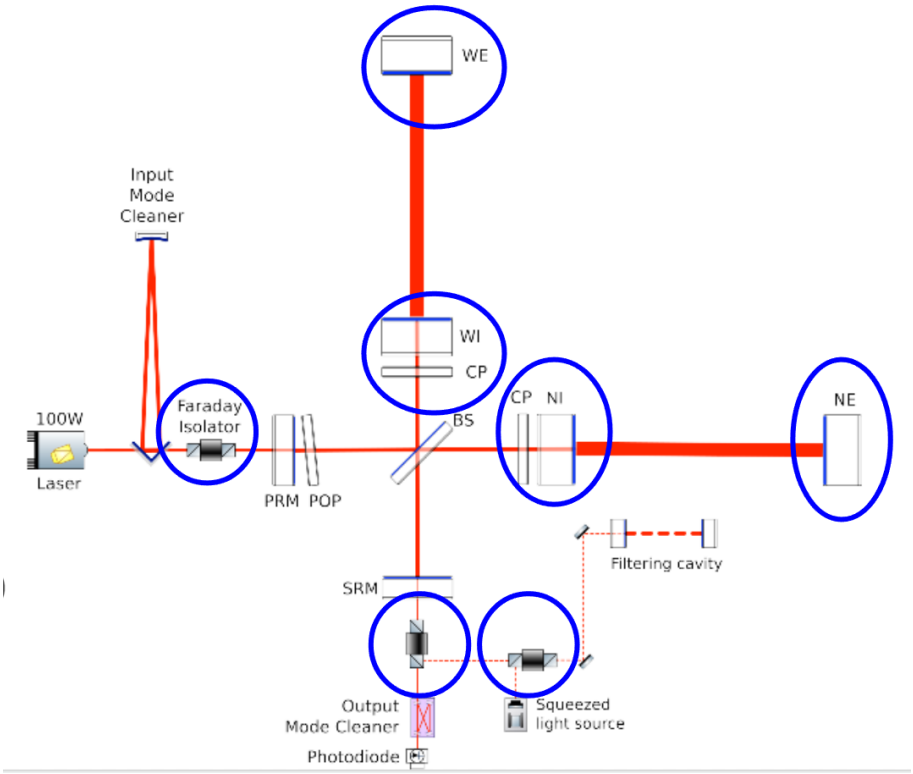

Figure 6: Virgo locations sensitive to magnetic field [6]

Note that, even if magnetic noise coupling at the mentioned locations might prove not to limit the present Virgo interferometer, it is important to study and test mitigation solutions because they might become limiting in the next generation of gravitational wave detectors, for instance the Einstein Telescope [5].

2 Faraday Isolator generalities

In this chapter, we focus on the Faraday Isolator, and we introduce the generalities of this component. [2]

2.1 Principle

Faraday isolators are used to avoid reflections of light going backward. It is used as an "optical valve". To perform this, a magneto-optic crystal is used. An example of crystal used is terbium gallium gernet (TGG), and these crystals have a high Verdet constant. The Verdet constant V quantifies the intensity of the Faraday effect, an effect that changes the polarisation angle θ in this type of material, depending on the magnetic field norm B and the optical path L. These variables are linked together by the equation :

$$\theta = VBL \tag{6}$$

That polarization rotation occurs in both directions. When coupled to a polarizer, it becomes possible to redirect beams going backwards.

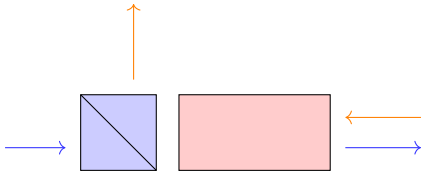

Figure 7: Principle of a Faraday Isolator

In figure 7, the polarization separator is indicated in blue, the magneto-optic crystal immersed in a magnetic field is represented in red, it rotates by $+45°$ the polarization plane of the beam. An incident beam of polarization $0°$ crossescrosses the polarizer, then the Faraday rotator where it gets $+45°$ polarization, and it gets out. A beam going backward of polarization $45°$ goes through the red first, attaining a polarization of $2\theta = 90°$, which is rejected by the separating cube in the upwards direction.

2.2 Magnetization distribution

The angle θ should be as high as possible for the Faraday performance to be maximal. The quality of the crystal determines the Verdet constant. The objective is then to maximize the magnetic field inside of the crystal. In order to do so, a magnetized cylinder is built around the magneto-optic cristal. (see figure 8)

A magnetic elementary dipole $d\overrightarrow{\mu}$ at a point M at a distance r creates at the origin of a system O the magnetic field :

$$d\overrightarrow{B} = \left(\frac{\mu_0}{4\pi}\right) \frac{3(d\overrightarrow{\mu}.\overrightarrow{OM})\overrightarrow{OM} - d\overrightarrow{\mu}}{r^3} \tag{7}$$

By parametrizing a side cut of the cylinder (taking into account axial symmetry) with a polar angle θ and the angle between the magnetization vector and the radial vector $\psi = \arccos\left(\frac{d\overrightarrow{\mu}.\overrightarrow{OM}}{|\overrightarrow{\mu}|r}\right)$, we obtain :

$$dB = \frac{M(r)d^3r}{r^3}\left(2\cos\theta\cos\psi + \sin\theta\sin\psi\right) \tag{8}$$

Which is then maximal when [7]:

$$\tan\theta = 2\tan\psi \tag{9}$$

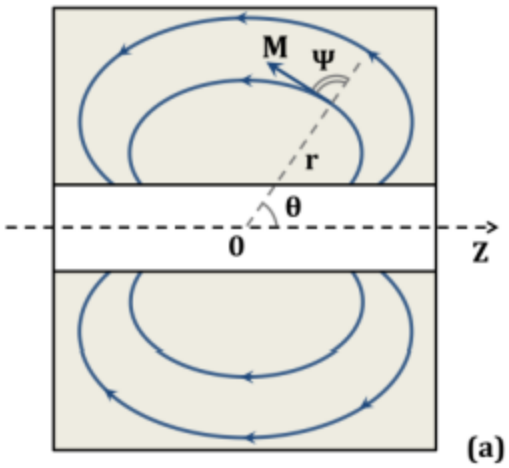

Figure 8: Optimal magnetization distribution for a Faraday isolator [7]

While this distribution is theoretically optimal for a Faraday Isolator, it is not realizable in practice.

2.3 Practical realization

The Faraday Isolator that was studied in laboratory was constituted of magnetized disks, mounted as a cylinder together. These disks tend to reproduce as much as possible the drawing of figure 8 in a limited amount of disks. It gives a magnetic field of $1T$ at the center of the faraday isolator. [8]

In particular :

- There is an axial symmetry of the magnetic field, thus there is no component of magnetization around the axis of the cylinder
- The radial and axial components should only depend on the distance to the center
- The magnetization can't be different inside of a disk in direction or in magnitude
- The disks are composed of several slices with unknown aperture angle

The actual number of disks and their magnetization is unknown for the commercial Faraday Isolators that are located on suspended detection bench (SDB1) and suspended injection bench (SIB1). The configuration adopted is one of those depicted in figure 9 :

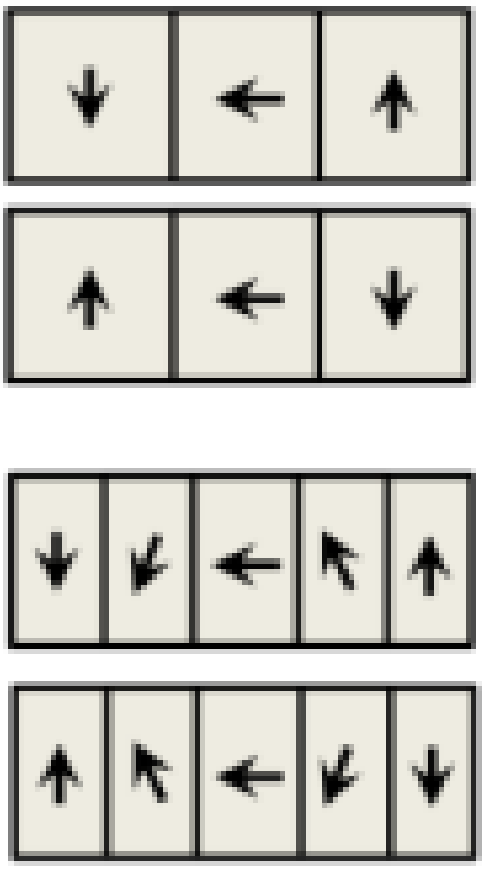

Figure 9: Possible magnet configurations for Faraday isolator [7]

3 Measurements and models of a Faraday isolator

The exact magnetization pattern in the magnetized cylinder is unkown, and to establish a model, a spare Faraday Isolator is studied. Measurements are performed to model the magnetic field of the magnetized cylinder.

3.1 Measurements

A spare Faraday Isolator (FI) of the model used on the suspended detection bench (SDB1) is placed on a granite optical bench. A magnetic probe is used to determine one component of the magnetic field in a point. A plastic support is designed, realized with a 3D printer and used to measure the two horizontal components by rotating the probe, with a $2mm$ accuracy on the point of measurement. The measurements, performed on a grid of points separed by $2.5cm$ and spread over a half-plane, cut perpendicular to the optical axis, are repeated with and without the Faraday Isolator. The support is shown in figure 10.

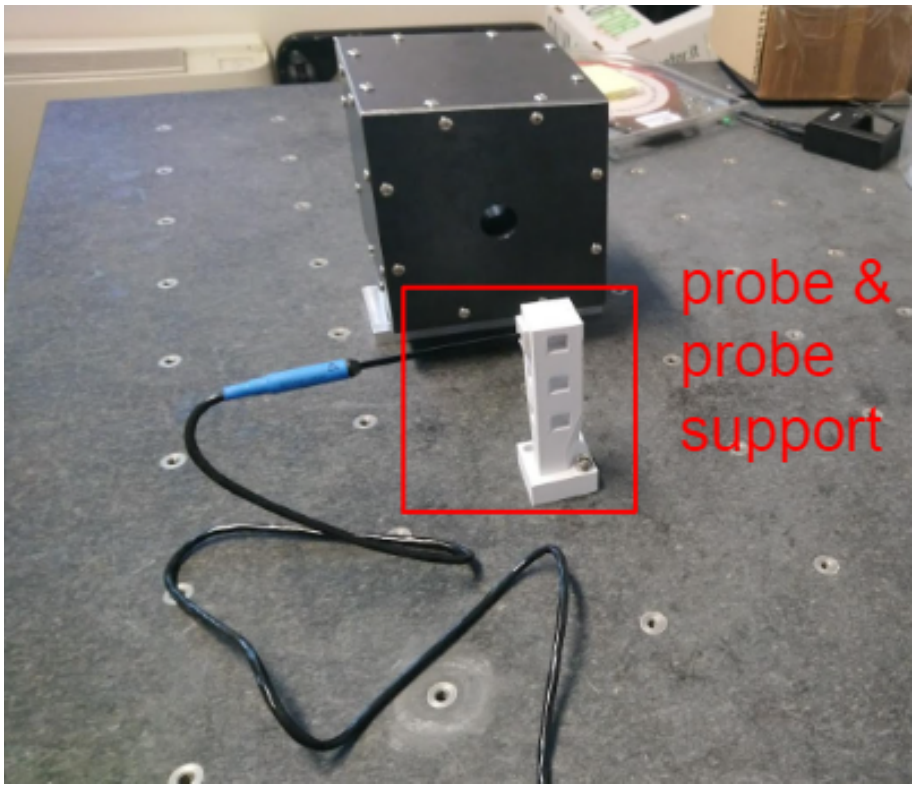

Figure 10: experimental measurement setup after the Faraday was encapsulated inside of a first magnetic shield (see chapter 9.)

Different models of Faraday Isolators are used in Virgo. The spare one is the same as SDB1 Faraday Isolator - which is $10cm$ long -, but the SIB1 Faraday Isolator is larger and has a magnetic field 1.5 times larger than the one on which measurements were performed. Due to the impossibility to conduct measurements on SIB1 bench directly, the measurements for the SIB1 Faraday Isolator are deduced from the SDB1 one by multiplying the results by a factor 1.5.

3.2 Experimental results

The results are extracted, and the magnetic field vector map is shown on a 2D map. A logarithmic scale is used to observe the pattern of the magnetic field. The results are presented in Figure 11 :

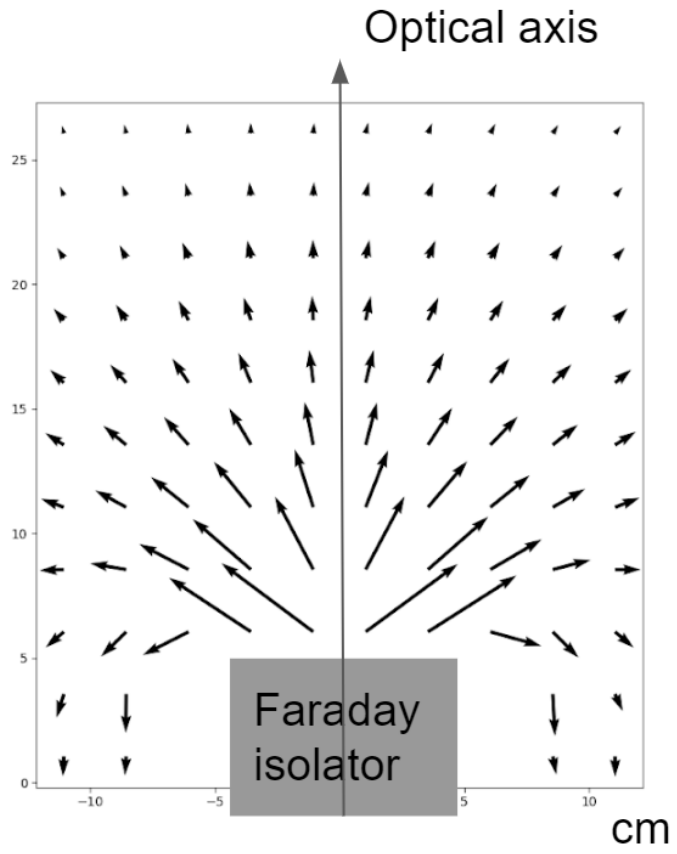

Figure 11: Magnetic field map for the Faraday Isolator

The magnetic dipole model is a good fit in far field, though it is very different in close field due to the magnetization being different on the border of the magnetized cylinder. There is an asymmetry with regard to the optical axis. This asymmetry was attributed to an offset error of the probe and the effect of the earth magnetic field. The earth magnetic field is substracted, then a check is performed by rotating the probe by 180 degrees to verify that the probe has an offset. This rotation gives a 10% error on the result which, combined with the earth magnetic field, corresponds to the observed asymmetry.

3.3 Dipole model

To determine the magnetic moment of our dipole model, the measured field in the area where the dipole model gives the best fit is used. Fractions of the full grid (containing 94 points) - called subgrids in the following - are then tested one at a time. The χ^2 is computed using the error of the probe reported in its data sheet on the measurement as standard deviation.

$$\chi^2(subgrid) = \sum_{subgrid} \frac{(\overrightarrow{B}_{dipole} - \overrightarrow{B}_{measured})^2}{\sigma_{probe}} \tag{10}$$

In that equation, the magnetic field predicted by the dipole model B_{dipole} depends on the position on the grid, and the equivalent magnetic moment $\overrightarrow{\mu}_{eq}$ that we attribute to the model.

The model we use has to respect the axial symmetry of a Faraday Isolator. For this study, we use a magnetized cylinder model, with a uniform magnetization such that the integrated magnetic moment is equal to $\overrightarrow{\mu}_{eq}$. This situation is then simulated for a unitary magnetic moment in a

simulation software, and the magnetic fields at each point of the grid are extracted. The results are shown in figure 12.

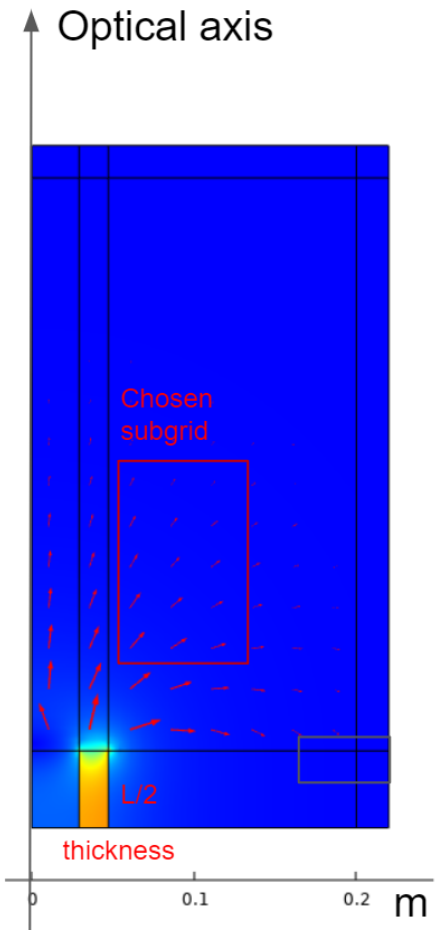

Figure 12: Axisymmetric model of the Faraday Isolator

For each subgrid, there is one optimal $\overrightarrow{\mu}_{eq}$ which gives a minimal value to χ^2. Various subgrids are tried and one is chosen in a region far enough to avoid the close field effects, and close enough to avoid limitations due to the probe accuracy. The optimal μ_{eq} value (norm of the equivalent magnetic moment) obtained is :

$$\mu_{eq} = 74Nm/T \tag{11}$$

3.4 Position dependant magnetization model

The previous model is very simple and matches experimental data. However, its result in close field range differ from what is observed in reality. Producing a more advanced model requires the knowledge of what is inside of the magnetized cylinder. That information was not available during the internship, but a program was written as a preparatory work to adapt this model. It relies on an axially symmetric magnetization, with no orthoradial component and with axial and radial components depending only of radius and axial position:

$$\overrightarrow{m} = m_r(r,z) + m_z(r,z) \tag{12}$$

The triangles composing the slices have an uniform magnetization. Thus, the slices are not

completely axisymmetric. The hypothesis of axisymmetry is still made, removing a dependance in θ of the magnetization.

4 Suspended injection bench (SIB1)

In this chapter, a magnetic simulation of the SIB1 is developped [2] using Comsol v6.0. The magnetic model explained in Chapter 2 is adapted as stated earlier. The entire SIB1 Faraday Isolator is then modelled as a magnetic dipole located at the position of the Faraday Isolator, oriented in its axial direction, and with a magnetic moment of :

$$\mu_{SIB1} = 74 \times 1.5 = 111 Nm/T \tag{13}$$

The objective of the simulation is to evaluate the force and the torque produced on the bench by an external magnetic field. In particular, a magnetic injection will be simulated to prepare for an experimental validation of the results.

4.1 Magnetic model

Two main physical phenomena are taken into account as stated earlier. The first one is the direct action of the external magnetic field on the magnetic moment corresponding to the Faraday Isolator. The second one is the induced currents.

The necessity to model a more complex geometry comes from the requirements on precision on the final results of the simulation. The direct effect happens only on magnetized parts of the bench and the tower to which the bench is suspended. The only permanent magnet on SIB1 is the magnetized cylinder of the Faraday Isolator. This cylinder is also the only ferromagnetic part on the bench. The magnetization induced by the external magnetic field on the magnetized cylinder is proportional to the external magnetic field, which is much smaller than the intrinsic magnetization of the cylinder. As a result, the induced magnetization on the cylinder will be neglected. The first effect of the magnetic field is thus only via the initially found magnetic moment of the Faraday Isolator. The induced effect, however, happens in every conductive component on the bench.

The magnetic field at the position of the Faraday Isolator is determined by averaging over the magnetic field on various points of a uniform 3-dimensional grid. The results are then extracted and put in a separate Python program made to compute the post-treatment force and torque calculations.

The two effect of Eddy currents, one by the Lorentz force, and the other by the modification of the magnetic field, both scale in frequency. A range of frequency, distributed logarithmically from $1Hz$ to $1000Hz$, is examined for this study.

As a result, the output of the simulation is, for every frequency :

- The magnetic field on every point of the grid around the Faraday Isolator
- The Lorentz force and torque contributions on the entire bench

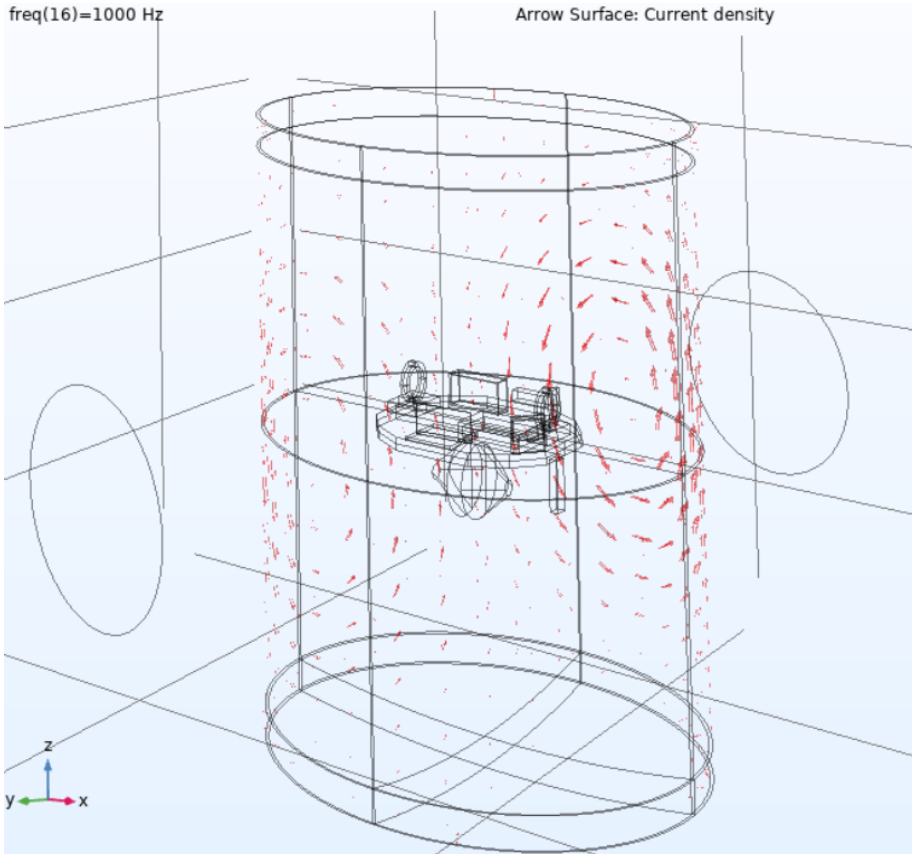

Figure 13: Eddy currents pattern in the simulation

4.2 Material model

In order to reconstruct the magnetic field correctly at the position of the Faraday Isolator, the characteristics of the used materials have to be added to the simulation. In particular, the magnetic permeability will used because of the shielding properties of several materials.

Moreover, the Eddy currents are the largest the lower the resistivity of the material. The effects induced are then stronger in more conductive materials, and thus these elements are important to be included in the simulation.

4.3 Geometric model

In order to reconstitute the contribution of the Eddy currents for the magnetic field and Lorentz contribution, it is essential to model very precisely the geometry, in particular of the following :

- Conductive components that are close to the Faraday : to reconstruct the local contribution on magnetic field
- All large or very conductive surfaces on the bench

The process of modelling the geometry of the bench was iterative. Pieces were added in order of decreasing surface and conductivity until the expected precision was reached.

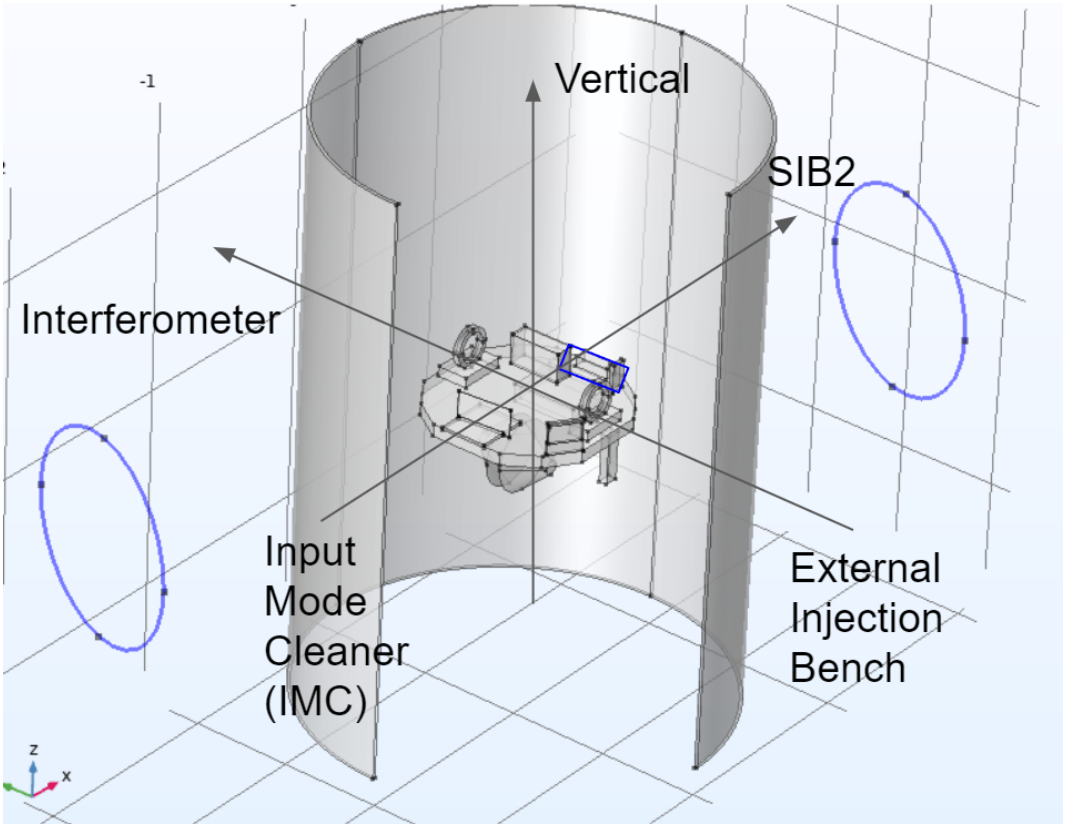

Figure 14: Simulated geometry

The first modelled part is the vacuum chamber (called tower) around the bench. As seen earlier, the bench is suspended inside the tower, and there are about 4 meters between the bench and the top of the tower. The scale of the bench (about a meter) and of the tower ($2m$ diameter) motivated us to consider the tower as an infinitely long steel cylinder of the same radii.

The support of the dihedron represented on figure 2 which reflects the beams within the input mode cleaner optical resonant cavity is represented due to its large surface and importance in the following.

The resonating cavity's conductive part are modelled as two fractions of cones. The inside part is not conductive and represented as air.

Other parts in copper and aluminium are also added to the simulation in order of surface. A particular attention was given to the parts close to the Faraday Isolator (inside the blue rectangle on figure 14).

The reference system, oriented along the axes of the interferometer, is indicated by the three arrows on the figure. The two injection coils are represented in blue.

4.4 Injection model

This section focuses on the source of the perturbation that we want to test on the bench. The interest is that, under the assumption that the environmental magnetic noise is on a larger scale than the bench, they will be uniform on that space.

As a result, the objective is to produce experimentally a magnetic field as uniform as possible.

As it will be developped later, two coils, as shown on Figure 14, are placed as close as possible to the tower, parallel and in anti-phase. These $50cm$ radius coils are modelled as a circular unitary current with unitary turn. This leads to the final results of the simulation in magnetic field, force

and momentum to be expressed respectively in $T/(A \times n_{turns})$, $N/(A \times n_{turns})$ and $Nm/(A \times n_{turns})$.

5 Simulation results

This section covers the results of the simulation and the post-treatment of these results.

5.1 Magnetic field results

The space occupied by the magnetized cylinder of the faraday is covered by a rectangular parallelepiped. The Faraday Isolator on SIB1 bench is rotated by an angle $3.5°$ with respect to the axis of Virgo. The grid is in the axis system of Virgo, and some points on the grid are thus outside of the Faraday Isolator. These points will be removed by further calculations. This grid contains 10 points in the axes that form a basis of the circular section of the Faraday Isolator, and 30 points in its axial direction, for a total of 3000 points.

The three components of the magnetic field are computed and saved for every point of the grid, and this for every frequency of the study, as well as one in stationary study ($f = 0$). The results are shown in figure 15 :

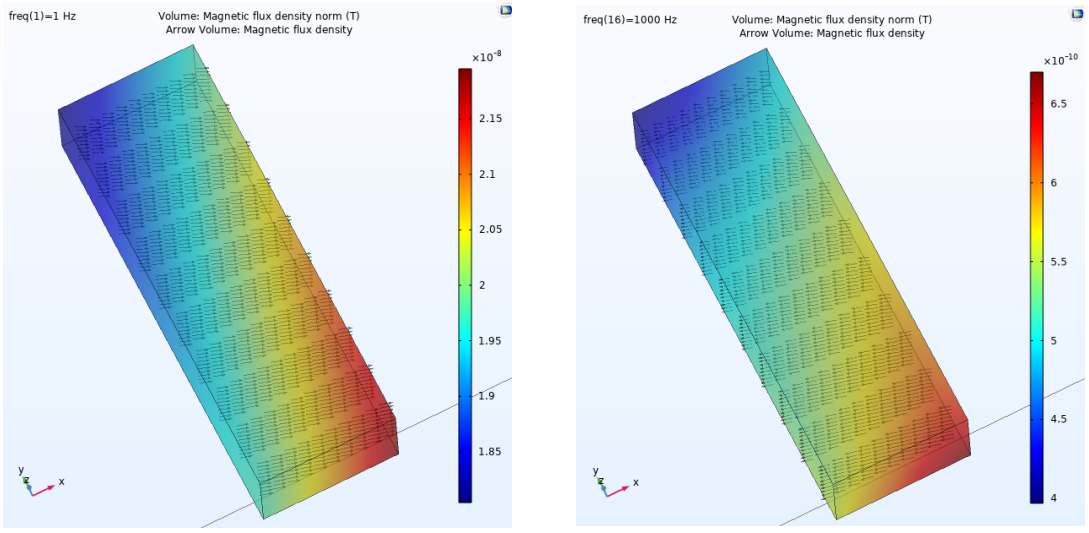

(a) Magnetic field at $1Hz$

(b) Magnetic field at $1Hz$

Figure 15: Magnetic field norm for the grid of points containing the Faraday Isolator on SIB1 bench

5.2 Force and Torque on Faraday Isolator

As explained earlier, the magnetization is supposed uniform on the magnetized cylinder of the Faraday Isolator. We name $\mathbb{1}_{cyl}(p)$ the function equal to 1 if the point p - in the grid of $P = 3000$ points defined ealier - is inside of the magnetized cylinder, and 0 everywhere else. This function allows to express the total force and momentum in our model by :

$$\overrightarrow{F} = \frac{1}{P} \sum_{p} (\overrightarrow{\mu}_{FI}.\overrightarrow{\nabla})(\overrightarrow{B}(p)) \tag{14}$$

$$\overrightarrow{T} = \frac{1}{P} \sum_{p} \overrightarrow{\mu}_{FI} \times \overrightarrow{B}(p) \tag{15}$$

The gradient itself is evaluated based on the assumption that the density of points is high enough to give a correct approximation, leading to the following expression :

$$F = \frac{1}{P} \overrightarrow{\mu}_{FI} . \frac{\overrightarrow{B}(p+1) - \overrightarrow{B}(p-1)}{2.h} \tag{16}$$

Where h is the distance between two points in the considered direction, and $p+1$ and $p-1$ are the next and previous points in that direction. This implicitly excludes points located on the frontier of that grid, where the force is not evaluated.

The force and torque components are represented in function of the frequency of the study in figures 16 and 17 :

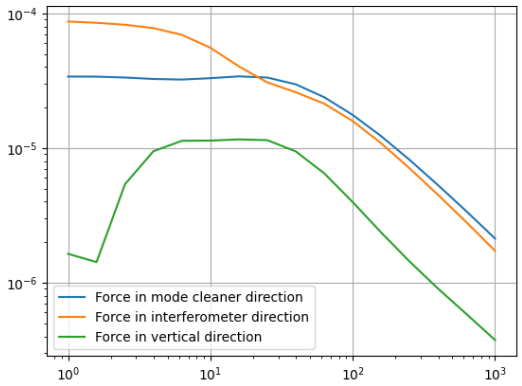

Figure 16: Force components as function of frequency (Hz)

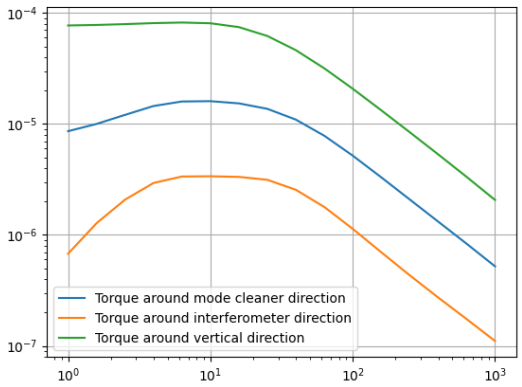

Figure 17: Torque components as function of frequency (Hz)

5.3 Force and Torque on bench

To determinate the force and torque on the entire bench, the torque has to be expressed at the center of mass of the bench. At this stage of the study, the effect of Eddy currents in terms of

Lorentz force are added to the previous part. The torque expression at the center of mass O, T_{com} is given in general as function of the torque expressed at the point M, T_M, by :

$$\overrightarrow{T}_{com} = \overrightarrow{T}_M + \overrightarrow{OM} \wedge \overrightarrow{F} \tag{17}$$

The contribution of the Eddy currents to the torque and force at the center of mass is calculated directly by the simulation software. The force and torque on the Faraday Isolator are manually computed using equation (18) with M being the center of the Faraday isolator. The center of mass is estimated using the executive designs of the bench. Results are shown on figures 18 and 19 :

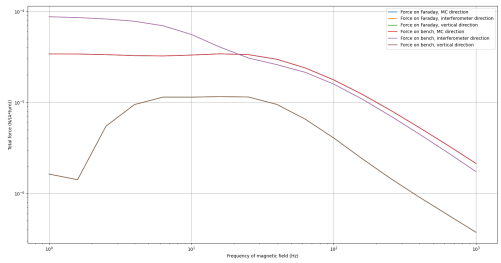

Figure 18: Force components on bench as function of frequency (Hz)

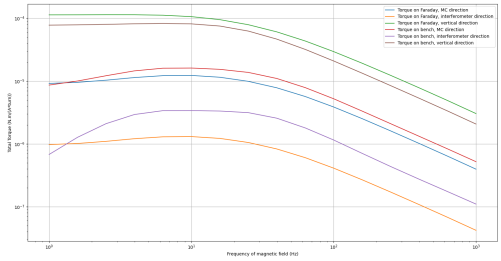

Figure 19: Torque components on bench expressed at the center of mass in function of frequency (Hz)

5.4 Displacement and rotations of the bench

The mechanical model assumes that the suspended bench behaves as a free-falling mass. This is true in the approximation that the mode of the pendulum are much lower than the frequency range of interest.

The SIB1 bench (and similarly SDB1) is suspended by three wires of length $L = 0.7m$ placed at the vertexes of an equilater triangle. Assuming that this system is equivalent to a pendulum :

$$f_0 = \frac{1}{2\pi}\sqrt{\frac{g}{L}} \approx 0.6Hz \tag{18}$$

The frequencies of interest are above 5 Hz. In that range of frequencies, it is assumed that the bench moves like a free mass. As a result, the displacement d is given by Newton's law :

$$d = -\frac{F}{m\omega^2} \tag{19}$$

And the rotation vector θ is given by :

$$\theta = \frac{1}{\omega^2} I^{-1} T \tag{20}$$

The obtained results are shown in figures 20 and 21 :

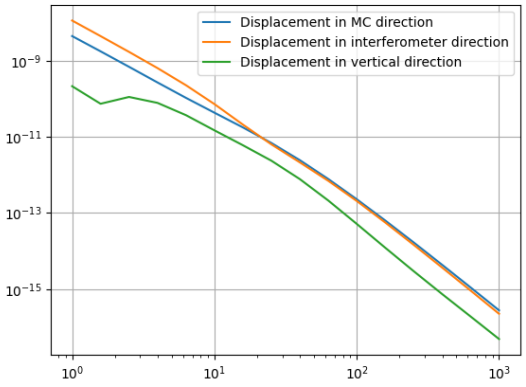

Figure 20: Displacement components of the bench as function of frequency (Hz)

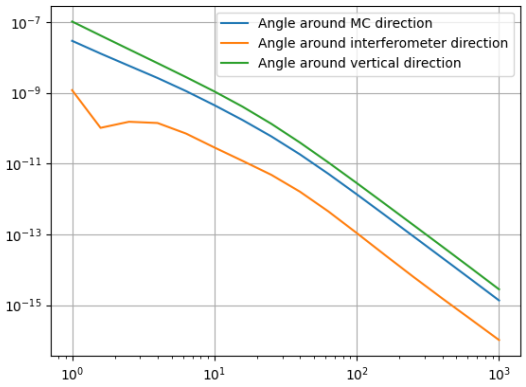

Figure 21: Rotation around the three axis of the bench as function of frequency (Hz)

6 Sensor – Reference cavity

This chapter describes the experimental verification of the results shown earlier. It introduces and focuses on the sensor used to perform this verification, the reference cavity.

6.1 Generalities

Taking into account the magnitude of the magnetic field involved, the expected displacement of the bench is very small. The most sensitive sensor to measure such displacement would be the interferometer. At the time of that study, the interferometer was in commissioning phase, and it was not possible to use it. Thus, in order to measure the displacement of the bench, another sensor specific to the SIB1 bench is used : the reference cavity.

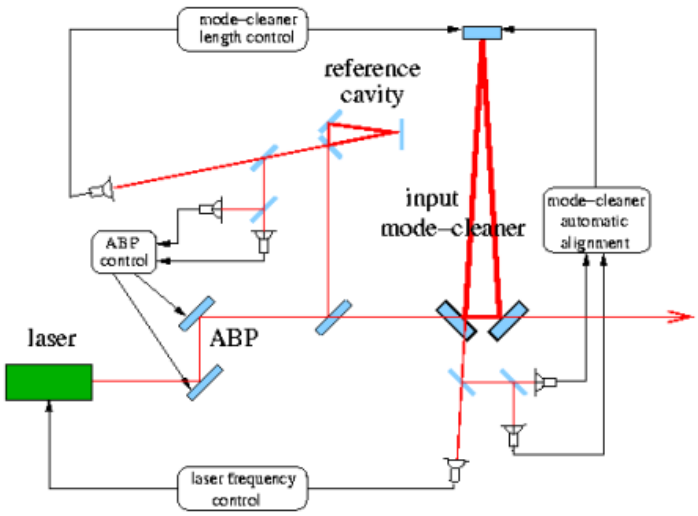

Figure 22: Optical scheme of the injection part of Virgo

The reference cavity is a device used to control the input mode cleaner length. The changes in the distance between the bench SIB1 and the mirror placed at the end of the 140m long input mode cleaner cavity is the open loop error signal of that reference cavity, used to control this distance. As a result, one can measure the displacement of the bench along the input mode cleaner (IMC) direction using this calibrated open loop error signal.

6.2 Calibration

To understand the calibration of that sensor, the simplified block diagram of the IMC control system is indicated in figure 23 :

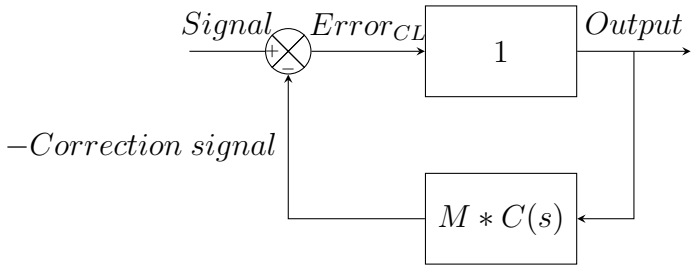

Figure 23: Block diagram of the Reference cavity control

As a result, the displacement is given by :

$$Displacement = Error_{OL} = (Error_{CL} - Correction\ signal) = Error_{CL} * (1 - M * C) \quad (21)$$

Where M and C are respectively the transfer functions for the mechanics and the corrector of the sensor. The purple line in Figure 24 shows the uncalibrated error signal of the IMC control. In the same plot the blue line shows the same signal when an external magnetic field excitation is applied, as explained in Section 7.

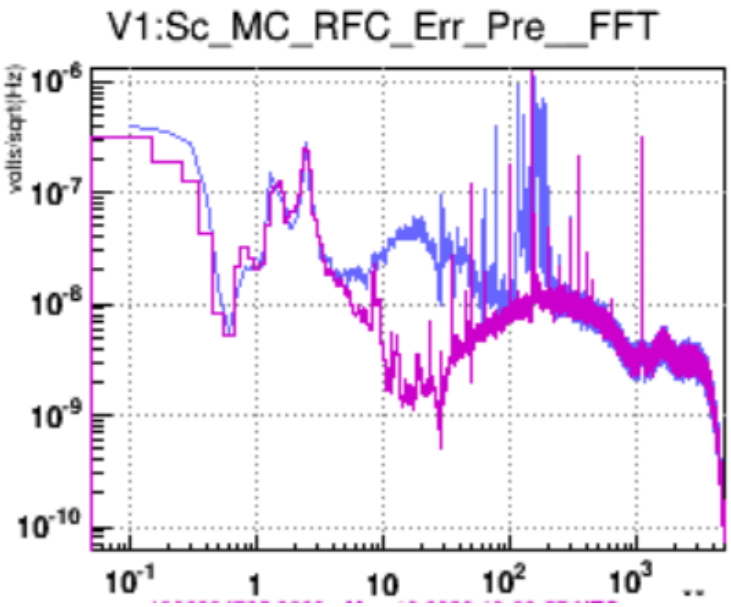

Figure 24: Uncalibrated signal of the reference cavity (purple) and when an external magnetic field excitation is applied (blue)

And by applying equation 22, the sensitivity of the calibrated sensor is obtained. By definition, it is the calibrated signal of the sensor, in absence of exterior injected noise. The result is show by the orange line in figure 25:

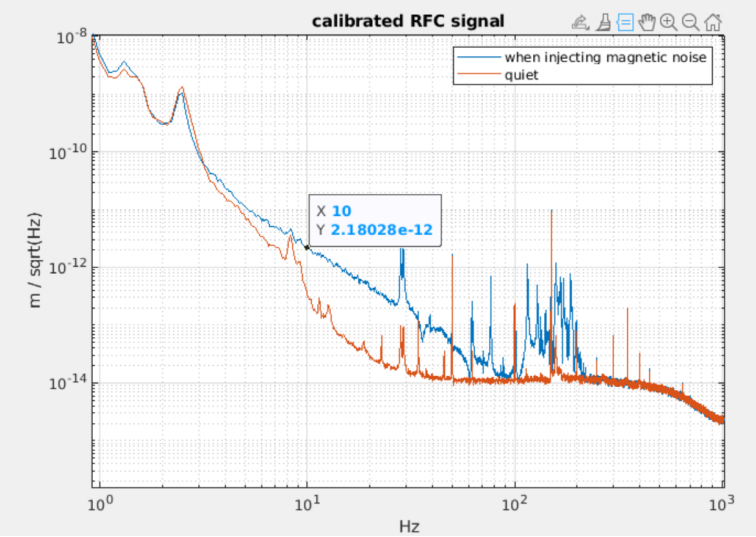

Figure 25: Calibrated signal of the reference cavity (orange) - sensitivity in $m/\sqrt{Hz}$ and when an external magnetic field excitation is applied (blue)

7 Experimental setup and results

7.1 Injection experimental setup

To produce a magnetic field inside of the tower, the following electrical components are used :

- a Digital to Analog Converter module which converts the given digital signal to an analog output (Volts) to the coils circuit
- an amplifier
- two coils
- various sensors : ampèremeter, magnetic Virgo sensors to control the magnetic field

The DAC module is driven by the Virgo user interface to send a controlled voltage in the circuit. The circuit itself is composed of the two coils of radius $0.5m$ and 50 turns of $1mm$ copper wire in anti-phase configuration forming a series circuit with the injection. It also involves several monitoring tools to test the experimental setup.

The space around the tower containing the SIB1 bench is very restricted, due to the presence of numerous infrastructures. The chosen configuration is shown in figure 26.

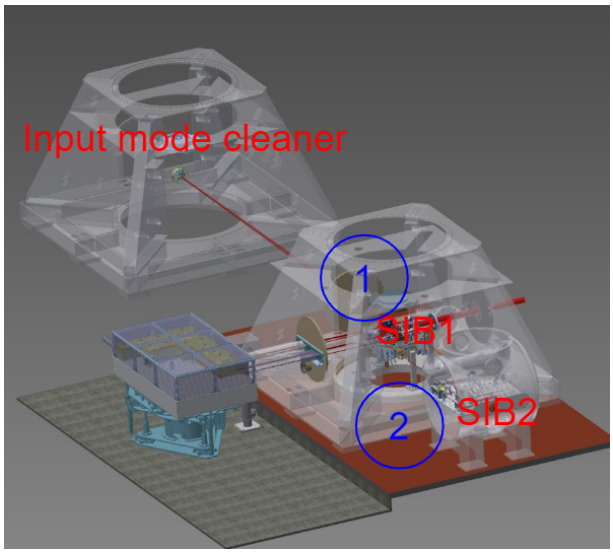

Figure 26: Positioning of the injection coils

The space where coil $n.2$ is positioned (Figure 26) is inside of a sealed clean room to which the cables of the electronic circuit can't be sent. The space where coil $n.1$ (Figure 26) is positioned on the interferometer side, opposite to this one, is thus also impossible to use because the two coils should be facing each other.

The space on the input mode cleaner side is occupied by multiple electronic devices, constraining the coil to be at least a meter appart from the tower. The space opposite to this one is next to another bench, SIB2, located inside of a clean room. The experimental setup is shown in figure 27.

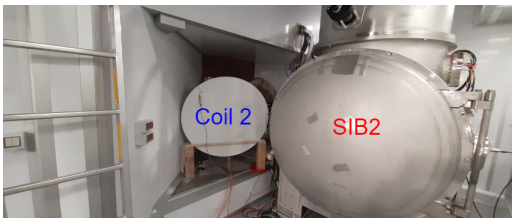

(a) SIB2 side

(b) Input Mode Cleaner side

Figure 27: Experimental setup

7.2 Injected noise

In order to obtain information on the movement on the bench for every frequency of interest, a white noise is injected.

The range of that white noise is chosen based on the results of the prediction detailed later. The final range is $f \in [5Hz, 195Hz]$.

The voltage, of chosen root mean square $0.05V$, is injected inside of the circuit after going through an amplifier where the injected current is monitored in real time during the experiment.

The injected voltage is shown in Figure 28.

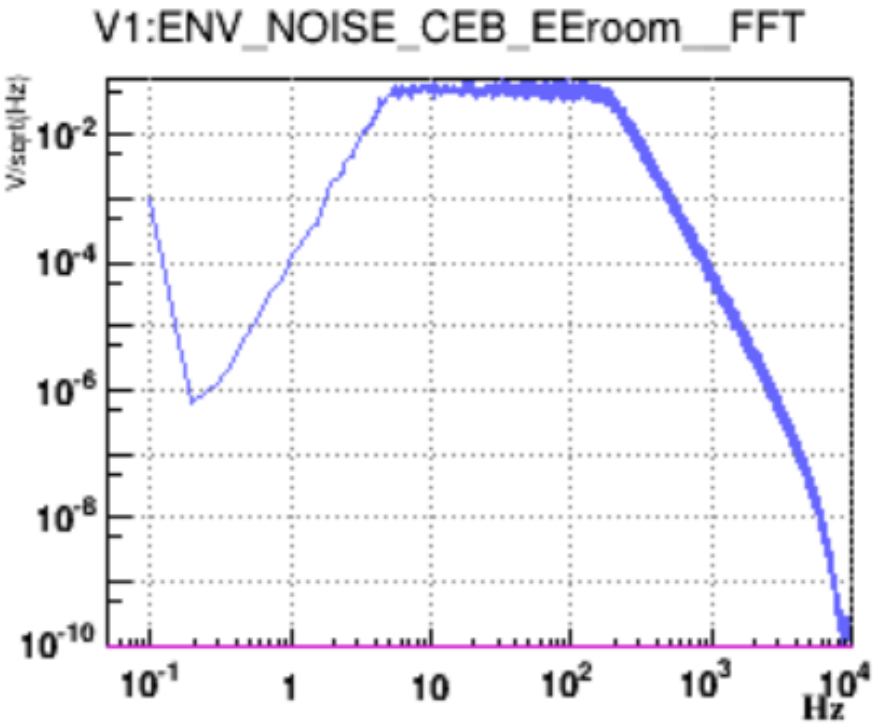

Figure 28: Tension on the coils during injection (blue)

The obtained current is shown in figure 29.

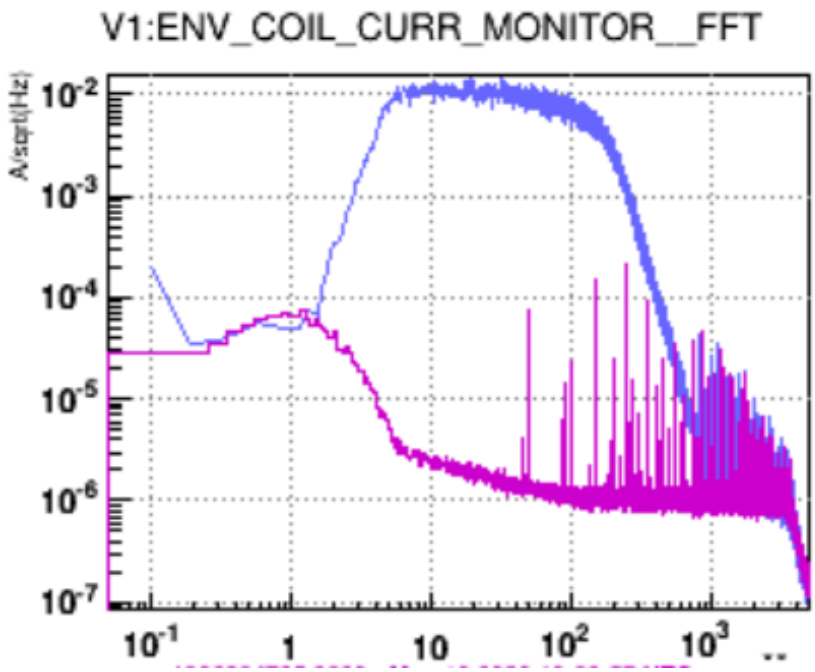

Figure 29: Current inside of the circuit during injection (blue) and amplifier's noise (purple)

7.3 Results

The previous current white noise distribution is modelled by a constant noise of corresponding amplitude and two cut frequencies, and multiplied by Chapter 5 transfer functions (figures 20 and 21) to obtain the predictions in terms of displacement and rotations of the bench.

The dihedron whose displacement $D_{corrected}$ is linked to the reference cavity error signal isn't at the center of mass of the bench (of displacement D_{COM}). The distance d between them implies the existence of an angular correction term to the displacement obtained previously.

$$D_{corrected} = D_{COM} + d.(\cos\alpha_{IF} - \cos(\alpha_{IF} + A_{IF}) \times \cos A_{Vertical}) \tag{22}$$

Where A_{IF} and $A_{Vertical}$ are respectively the angles of rotation of the bench around the interferometer axis and the vertical axis.

This corrected displacement is the prediction of the model for the error signal of the reference cavity.

After the calibration process detailed in chapter 6, the results are shown in figure 30 [2]

[2]The results shown for the simulation model do not take into account the level of noise of the reference cavity sensor, explaining significative difference when the sensor noise level is high with regard to the prediction

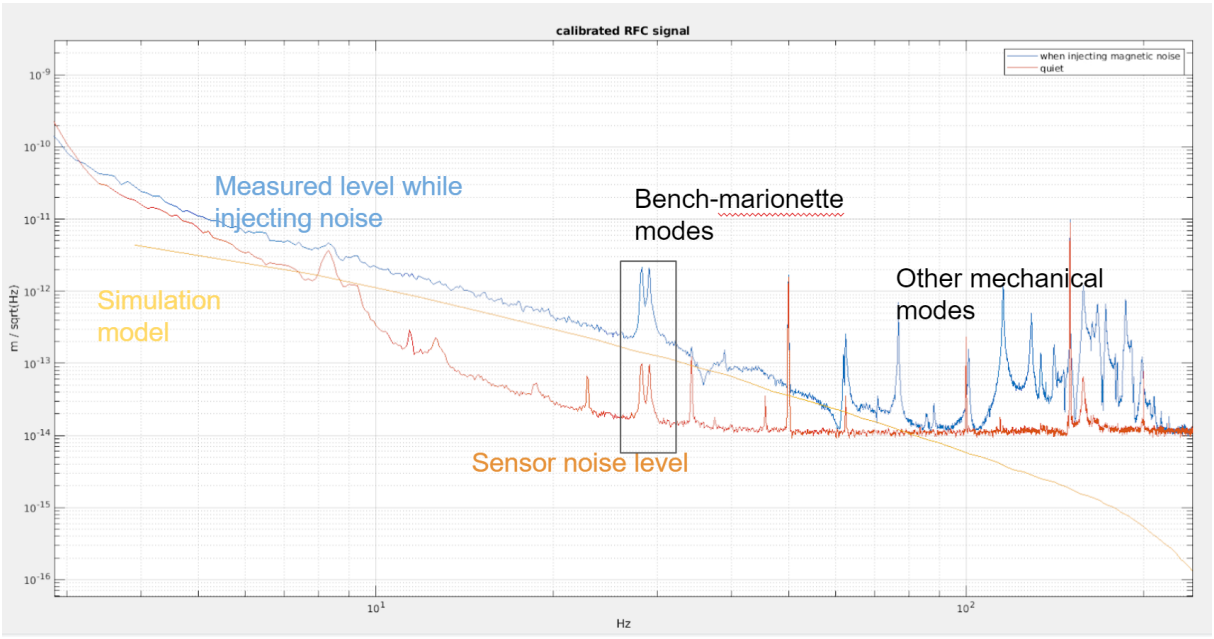

Figure 30: Measured displacement of the bench (in blue) confronted with sensor sensitivity (in purple) and model prediction (in yellow)

The model prediction is a factor 1.7 under the observed results. The sources of error leading to that discrepancy and potential solutions are listed in chapter 10.

Two of the peaks present on figure 30 around $20Hz$ were identified as being the system resonances between the bench and the upper part of the tower used to control the bench, called marionnette. The higher frequency resonances require further analysis which is out of the scope of the internship, but are believed to be caused by the support of the dihedron's flexibility and rotations resonances.

The study confirms the results of the model in the investigated domain of frequencies, and in particular its sensitivity to external magnetic field.

8 Shielding generalities

This chapter focuses on a solution of passive shielding of a permanent magnet and its application to the SDB1 bench. The first objective is to diminish the coupling of the bench to external magnetic field. The second objective is to protect a sensitive magnetic component present on SDB1 bench, a fast shutter, from the magnetic field of SDB1's faraday isolator. The fast shutter consists in an absorbing glass mounted on a magnet that elevates itself with a coil to block the laser beam when the interferometer loses control. It is especially sensitive to magnetic fields that might affect its elevation phase. These objectives are part of the phase II upgrade of the Advanced Virgo detector.

8.1 Effect of magnetic permeability

Permeability is the first aspect of passive shielding. Materials have a magnetic permeability μ, which characterizes their capacity to modify the magnetic field lines. For ferromagnetic material in general, the permeability becomes lower for high magnetic fields, but remains linear for small magnetic fields, as shown in Figure 31. The higher the value of μ, the more the field lines will be

affected by the presence of that material. The magnetic field inside of the screen can be determined by solving the Maxwell equations. As an illustration, we consider a spherical screen of internal radius r, thickness t and permeability $\mu = \mu_0\mu_r$, immersed in a uniform magnetic field $\overrightarrow{H_0} = H_0\overrightarrow{e}_z$. When the currents are not considered, we can exhibit a magnetic potential Φ_M such that :

$$\triangle \Phi_M = 0 \tag{23}$$

By symmetry around z, the potential is expressed in terms of the Legendre polynomials :

$$\Phi_M = \sum_{l=0}^{+\infty} \left(A_l r^l + \frac{B_l}{r^{l+1}} \right) P_l(\cos\theta) \tag{24}$$

By using $\overrightarrow{H} = -\overrightarrow{\nabla}\Phi_M$ and $\overrightarrow{H_0} = H_0\cos\theta\overrightarrow{e}_r - H_0\sin\theta\overrightarrow{e}_\theta$, the magnetic potential outside of the screen is found to be $\Phi_M = -H_0 r\cos\theta$. We can then solve the boundary conditions at an interface of normal $\overrightarrow{n}$ between two spaces I and II, to finally obtain four equations (two inside and two outside of the shell) :

$$(\overrightarrow{H}_{II} - \overrightarrow{H}_I) \times \overrightarrow{n} = \overrightarrow{0} \tag{25}$$

$$(\overrightarrow{B}_{II} - \overrightarrow{B}_I).\overrightarrow{n} = 0 \tag{26}$$

By doing so, only the term of $l = 1$ in the series remains. The existence of non null $B_{1,shell}$ and $B_{1,inside}$ implies a reduction factor between the inside and the outside. The following expression for that factor $H_{inside} = \alpha H_{outside}$ is found :

$$\alpha = \frac{9\mu_r}{(2\mu_r+1)(\mu_r+2) - 2\left(\frac{1}{1+\frac{t}{r}}\right)^3(\mu_r-1)^2} \tag{27}$$

Which corresponds to the intuition : the factor α is smaller for higher thicknesses of the shell and higher permeability. This example, albeit much simpler than reality, where geometry is much more complicated and the induced currents inside the screen are not negligible, motivated the design of a passive shield as simple as possible made of high permeability metals.

8.2 Material characteristics for shielding

The constitutive relation $B = \mu H$ is a linearisation for low magnetic fields. Considered the large ($> 1T$) magnetic field of the Faraday Isolator, the saturation of the materials (permeability decreasing to 0 for fields of large intensity) has to be taken into account. In particular, for certain materials like μ-metal, this saturation can be as low as $0.5T$ (see figure 31). In that case, the linear model has to be replaced by a more complex one, including the variation of the permeability as function of H. Such a model is represented by a $B - H$ curve.

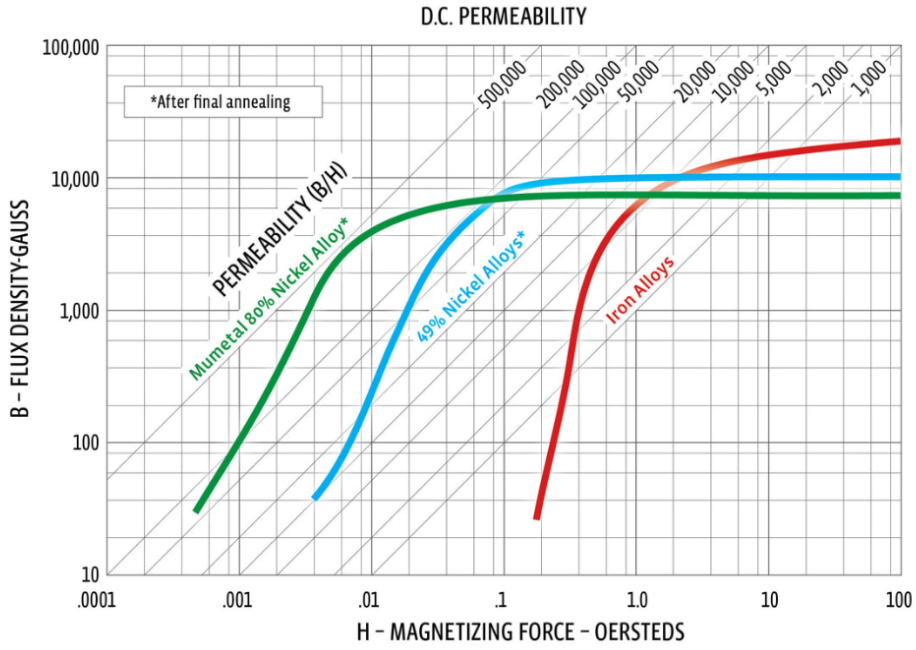

Figure 31: Constitutive relation for μ-metal

The first material used is iron. It is known to have high saturation (about $2T$), and good permeability at low magnetic field ($\mu_r = 5000$). A first screen was made of iron, and will be described in chapter 9. Another type of iron, with low carbon content, named "Ultra pure iron", was also used for that study. Their $B - H$ curve is indicated in figure 32:

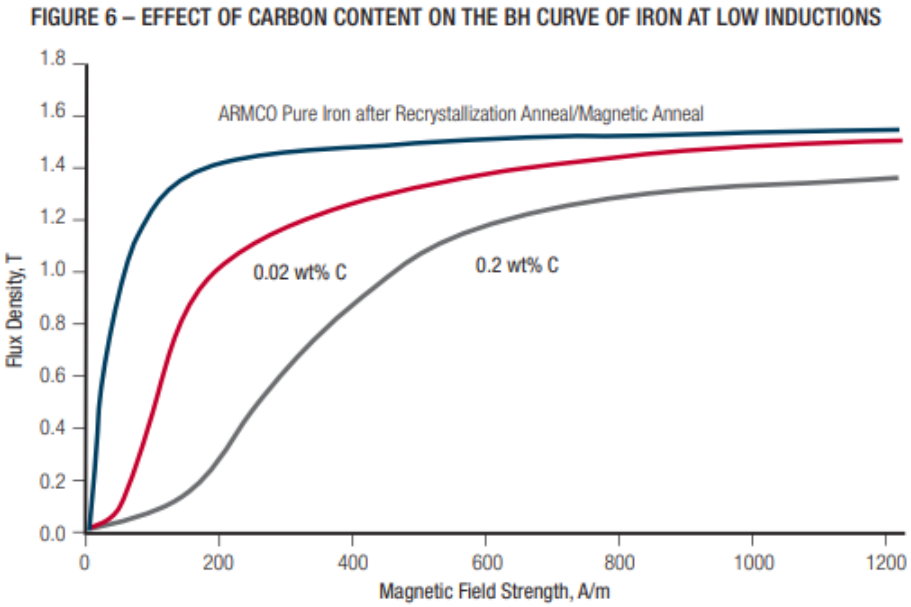

Figure 32: Constitutive relation for iron

The other metal we used for shielding is μ-metal, for its very high permeability $\mu_r = 100000$ at low magnetic fields. Its saturation is lower, and the full constitutive relation for this material is shown in figure 31.

The low saturation means μ-metal's shielding efficiency will be optimal if the field to which it is exposed is low. As a result the final shield design will have two shield layers, the inner one, being of iron to avoid saturation, the outer being of mu-metal.

8.3 Eddy currents

For high frequency fields, the Eddy currents can provide effective screening action. The induced magnetic field they create opposes itself to the initial magnetic field, and increases in intensity at higher frequencies. As mentionned earlier, it scales with conductivity of the material. Thus, conductive materials are used in the screen, to improve higher frequency mitigation. In particular, we will use aluminium.

9 Faraday shielding on suspended detection bench (SDB1)

This chapter presents the steps of elaboration of a magnetic shield for SDB1 Faraday isolators following the principles exposed in chapter 8. A particular attention will be given to the simulations and experiments done to validate the predictions.

9.1 First shield and simulations

The simplest shield possible was simulated, then realized, to test the agreement between experimental measurements and simulation results.

This first prototype consists in a rectangular box shape, with two holes on the front and the back side for the beam passage. The box sides are held together using metal screws inside of plastic rectangular supports that are placed on the internal side of the edges of the cube.

This screen was modelled in the simulation software. The Faraday isolator is modelled as a geometrically fitted uniformly magnetized cylinder as explained in chapter 3. The screen is modelled as a perfect box, without taking into account the plastic supports and the screws. The $B - H$ curve of the standard iron is used (see figure 32). A picture of the simulation is shown in figure 33.

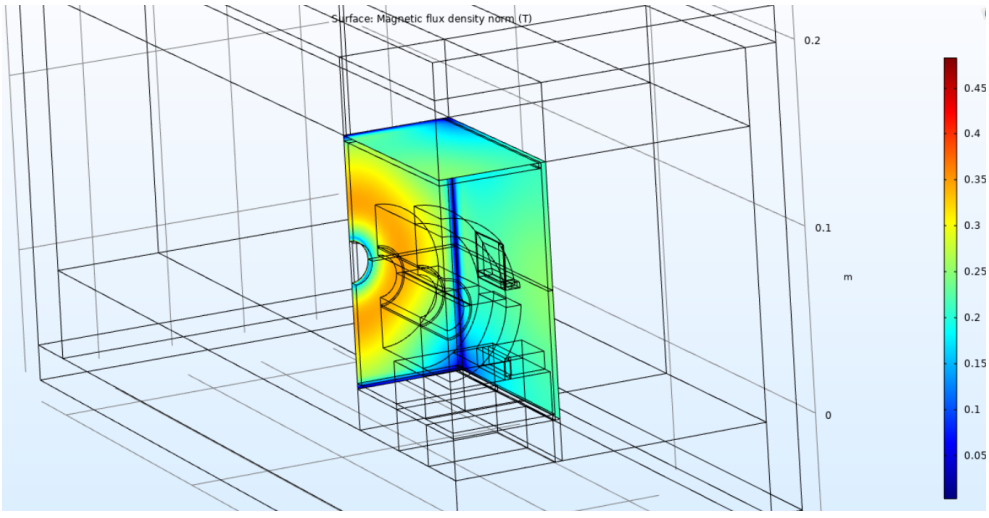

Figure 33: First screen simulation - with symmetries, only a quarter of the space is represented

The output of this simulation is the magnetic field map outside of the screen. To evaluate its shielding factor, a criteria based on the objective to reduce the magnetic field at the position of the fast shutter is used. The shielding factor η is then equal to the ratio of the norms with and without screen :

$$\eta = \frac{B_{no\ shield}}{B_{shield}} \tag{28}$$

In the case of that screen, the simulation result is $\eta_1 \approx 56$. The objective is $\eta > 100$. The objective is then to both create a shield that respects space constraints of the SDB1 bench, as well as a better performance. For this purpose, an optimisation is performed in the following.

The screen was realized (see figure 10), and the experimental result gives $\eta_{1,exp} \approx 49$. The technical drawing of the screen is shown in figure 34.

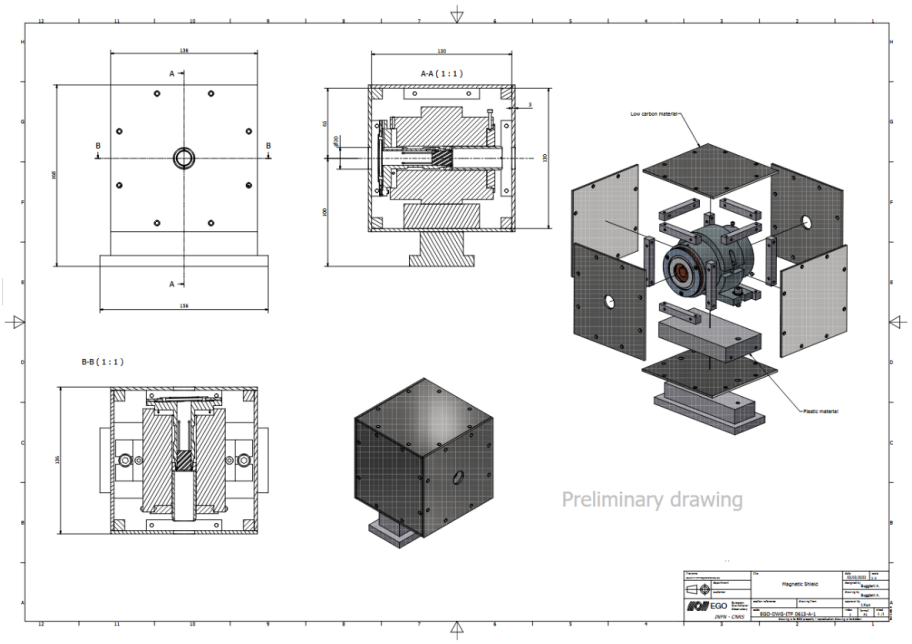

Figure 34: First screen around Faraday Isolator

9.2 Screen optimisation

In order to improve the attenuation factor, two layers of materials are used. The inner is ultra pure iron and the outer is μ-metal. The overall shape of the screen is changed to adopt a cylindrical shape and get closer to the Faraday Isolator.

Different methods of optimisation were tried. In particular, topology optimisation gave a non-realizable result by densifying the screen on the angles and leaving unconnected parts. This topology optimisation, not shown here, motivated the addition of strips of iron to cover the gaps at the edges of the cylinders. These gaps were shown to possibly worsen the result by a factor 2 in some cases. In order to produce a realistic screen, surface optimisation and topology optimisation are abandonned to choose a method giving simpler solutions, i.e. the parametric optimization method,

The shape of the screen is this time fixed. Different shapes were tried, in particular some of them with rounded angles, but were abandonned for realisability issues too. The chosen shape is that of two cylinders corresponding to the two layers : ultra-pure iron and μ-metal. The internal edges of the inner cylinder are covered by circular strip with triangle section. An axisymmetric view - from which the 3D model is obtained by rotation around the indicated axis - of that shape is shown in figure 35.

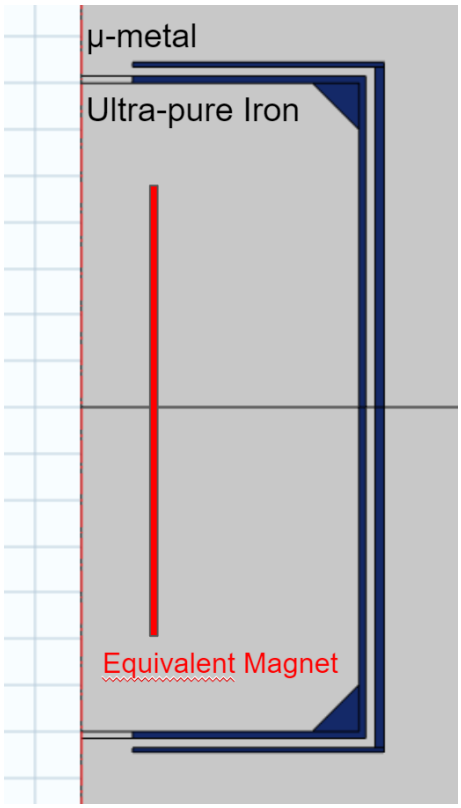

Figure 35: Axisymmetric view of simplified screen shape

The following parameters are chosen for this geometry.

- length of the internal cylinder
- width of the internal cylinder
- front and back thickness of the internal cylinder
- lateral thickness of the internal cylinder
- length of the ”triangles” on the internal edge
- front and back thickness of the external cylinder
- lateral thickness of the external cylinder
- space between cylinders

Thicknesses are fixed due to the market availability of the material used, in 1.5mm foils for iron, and in 1mm foils for μ-metal. The same applies to the space between the two cylinders, which is handled later.

Three parameters remain for optimization, length and width of the internal cylinder and length of the ”triangles” on the internal edge. This optimization is performed by using a parametric sweep over all possible parameters range, having assigned the geometric constraints detailed in the next subchapter. By iterating the study over all these values, a 4-dimensional map is obtained. The screen is found to give the best results when it is the closest to the Faraday Isolator. The results are then shown assuming the optimal width value on figure 36.

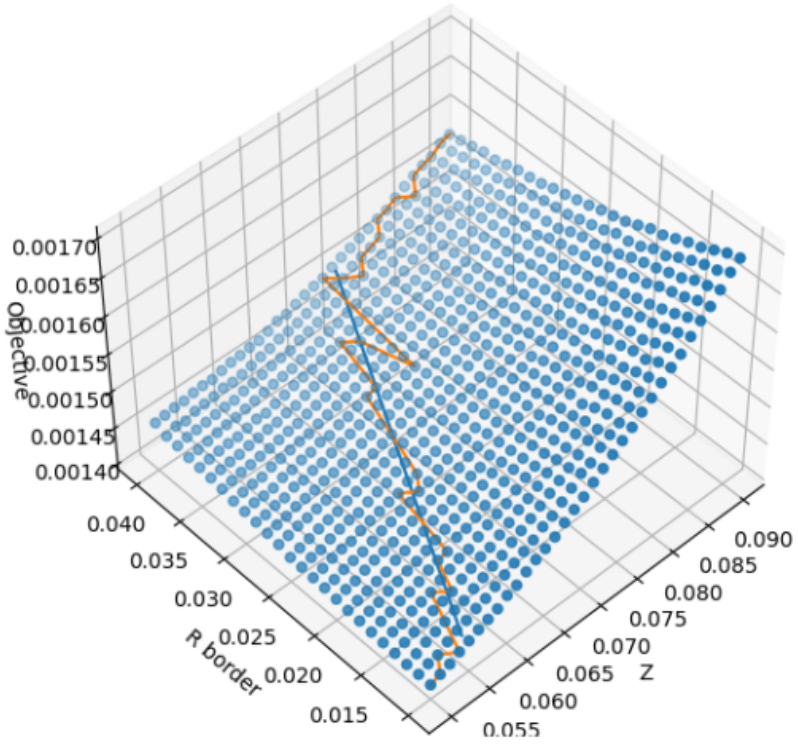

Figure 36: Normalized attenuation factor in function of length of the triangles and the cylinder

The optimum length of the triangles R at given geometry is then linearized, giving :

$$R = 1.54 * Z - 0.07 \tag{29}$$

The final R is then determined to give a better shield, and the other parameters are manually ajusted amongst the possible options. The final shield is then simulated with a more detailed model of the SDB1 bench surrounding it to give more reliable results. Unlike the previous chapters, the interest is focused on the parts around the faraday isolator and between this component and the fast shutter. The parts that are only taken into account as geometrical constraints are represented by their convex envelope. This simulation is shown in figure 37.

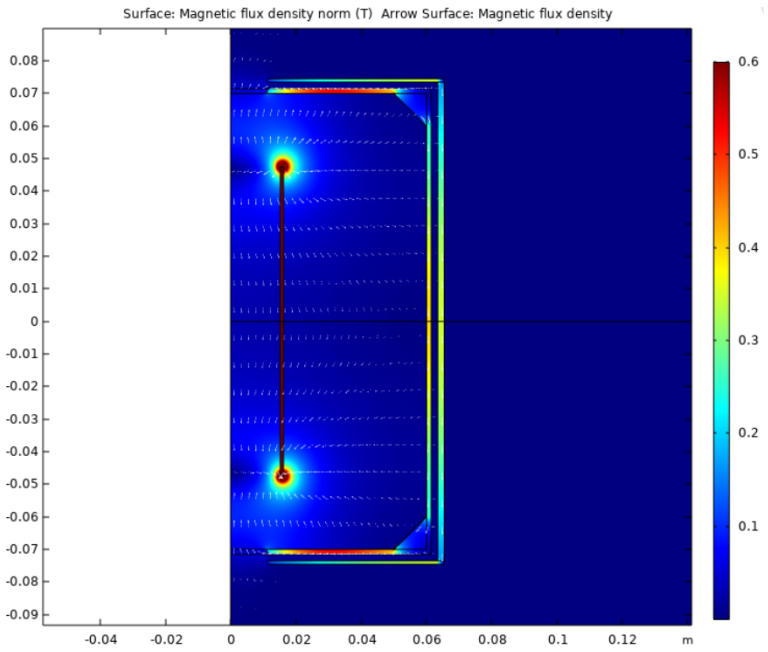

Figure 37: Optimized screen simulation

This simulation gives an attenuation factor $\eta \approx 200$. The next subchapter covers the adaptation of that screen to the constraints of the bench.

9.3 Adaptations to bench constraints

There are four major constraints to take into account :

- The external geometry : in close proximity of the faraday isolator, there is one mirror support, and two other optical components in the front and in the back
- The internal geometry : angles reinforcements must not touch the cylinder
- The position of the faraday isolator's crystal must be adjustable inside of the screen
- The cooling system which takes out the heat produced by the beam inside the faraday isolator must function correctly

The constraints are illustrated on figure 38.

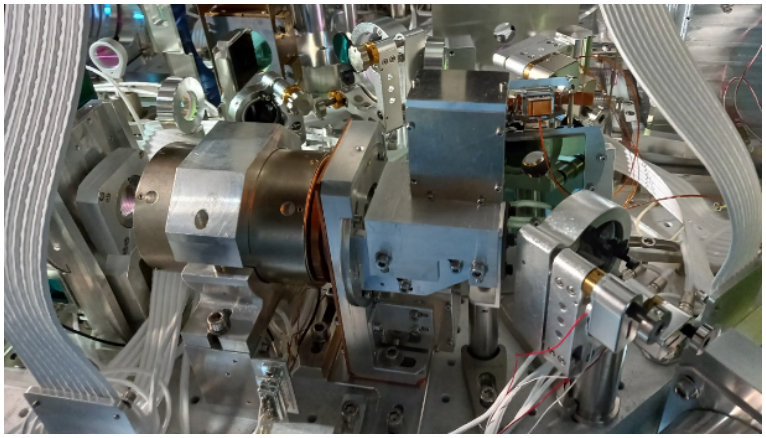

Figure 38: Picture of the faraday isolator on the SDB1

To take into account the first two constraints, the screen is redimensionned to fit in the available space. The initial support is not adapted to a cylindrical shield, and another support is designed. By modifying the length of the cylinder, the second constraint becomes unsatisfied, and the angles reinforcement have to be removed from the back of the faraday isolator.

The third constraint is satisfied by the addition of rolls in the space between the cylinders, widening this space.

The fourth is handled by putting a hole around the cooling plate on the bottom of the screen.

9.4 Last simulation and expected results

The final screen prototype obtained is shown in figures 39 and 40.

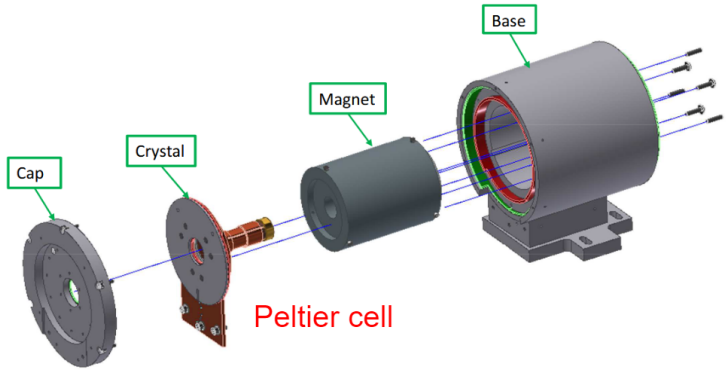

Figure 39: Final screen decomposed view

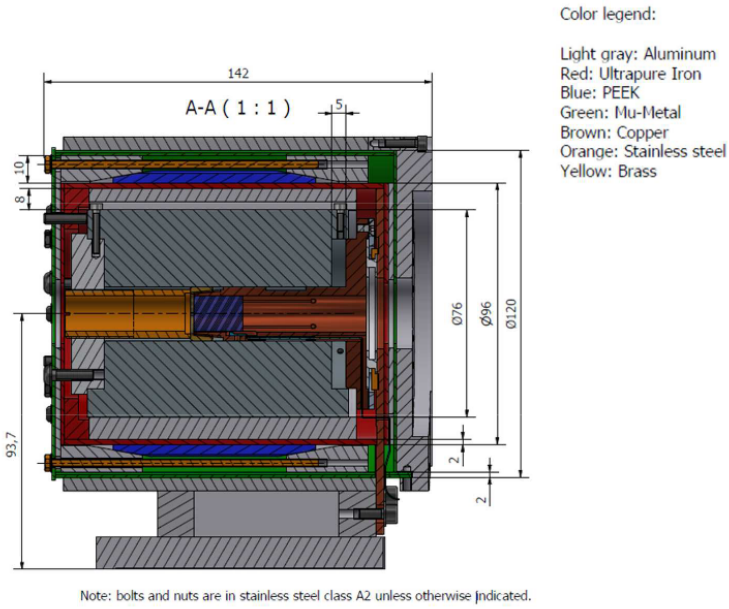

Figure 40: Final screen side view

This final screen is then inserted inside of the previous screen simulation. The final simulation is shown in figure 41.

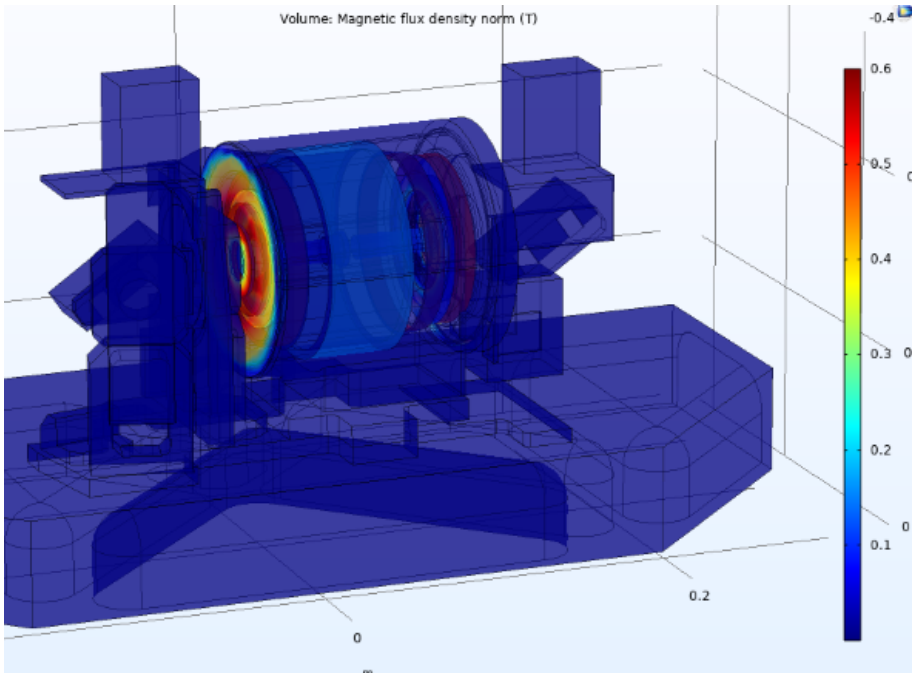

Figure 41: Final simulation of the screen

This magnetic shield gives a final attenuation factor of $\eta_{final} = 165$, which satisfies the expectation for this study in terms of protection of the fast shutter. At the time of the redaction of that report, the shield prototype is in production, and the measures of its attenuation factor are not available. The measure of the coupling to an external magnetic field is also yet to be performed.

Conclusion and next steps

This study covered different aspects of the environmental noise physics and experimental physics at Virgo. It presented the measurement of the effect of an external magnetic field and the realization of a practical solution to guarantee the functioning of sensitive optical components like the fast shutter, and to limit the effect of these fields on the sensitive parts of the interferometer.

During this study, the injection practical details are studied and realized. The injection process is elaborated, simulated on the SIB1 bench and the results of the simulation verified in practice. The response of the bench to the external sollicitation is quantified and compared with the expectations. The method of measurement is validated. The results show that the studied type of coupling can have an influence on the benches, and motivates the implementation of mitigation solutions in the future. A mitigation solution for the SDB1 bench faraday isolator is then studied, to mitigate both the effect of the external magnetic noise on the bench, and the effect of the faraday's magnetic field on the fast shutter. The faraday isolator's magnetic field is measured and modelled, and the results are implemented inside of a partial SDB1 simulation from which a magnetic shield around the faraday isolator is designed. This magnetic shield is then adapted to correspond to the experimental requirements and the efficiency objective.

This study triggers further measurements and interests around this subject. The method employed to measure the bench's behaviour measured the bench's displacement for a magnetic field produced by the two coils in the specified direction. The magnetic fields that affect the interferometer on a large scale are approximately uniform on the scale of a bench. However, their direction depends on the position of the source of that magnetic field. Thus, the study must be repeated for an injection at other angles on the bench. The output for every direction could then be extrapolated by a linear approximation from these two studies. The study should then be adaptable for every direction of magnetic field using this model, in the hypothesis that the magnetic field is uniform on the bench size scale. For smaller scale fields, a more in-depth study is required. The results should then be combined with the observed magnetic fields at the site. By using the magnetic sensors, one can then apply the transfer functions given by this study to estimate the movement of the benches. This step requires complementary studies and noise hunting[3]. An example of a noise hunting study is given in appendix.

The internship held place during a commissioning phase of the Advanced Virgo interferometer. A next step would be to reproduce the injection while using the interferometer, in order to obtain the effects of these injections on the measured DARM. This would allow to produce a projection of the environmental noise on the Virgo sensitivity. Eventually, the study described in this work would be reproduced in every sensitive place of the interferometer to establish a noise budget for the magnetic noise for the interferometer.

[3]Noise hunting is intended the characterization of the noise (in the specific case the magnetic fields) at the interferometer site, including the identification and mitigation of the sources.

Appendix - Hunting of a major source of magnetic noise at the Virgo site

This appendice presents a parallel activity conducted to identify the source of a magnetic noise that was observed on external magnetometers on Virgo site. These magnetometers have the objective to identify the Schumann resonances, at around 7Hz and higher modes. These are the resonances of the optical cavity formed between the surface of the earth and the ionosphere, excited by the lightning discharges all around the world. They are very subtle - of the order of $1pT$ - and require the sensors to have very low intrinsic noise and the environmental background noise to be very low to be observed. Since July 13th 2020 on these sensors appeared a noise band moving between 3Hz and 5Hz, and its harmonics. This noise was in the range of 100nT, much more intense than the Schumann resonance, hiding them completely. The observed spectrogram is shown on figure 42

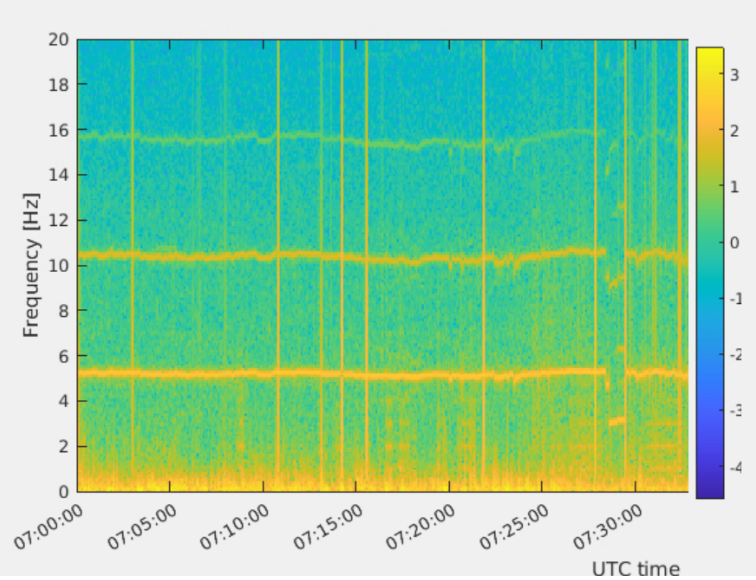

Figure 42: Spectrogram seen by the external magnetometers

An initial campaign of measurement using a portable magnetic probe and data acquistion system found the magnetic field was higher next to the metallic structures of Virgo, especially the outer side of the tunnels. This campaign was then prolongated to the entire Virgo side, to check for potential spots where the magnetic field was more intense. A spot of very intense (two orders of magnitude over what was seen on the rest of the site) magnetic field was found next to the entrance of the site.

Later on, this spot was identified to be on the path of a buried methane pipeline. This pipeline was then followed in both directions and found that the intensity of the magnetic field varied along the pipe.. The variation was found to be rather small and erratic, leading to think that the pipeline was acting as a local amplifier of the noise. The results of that campaign are shown on figure 43

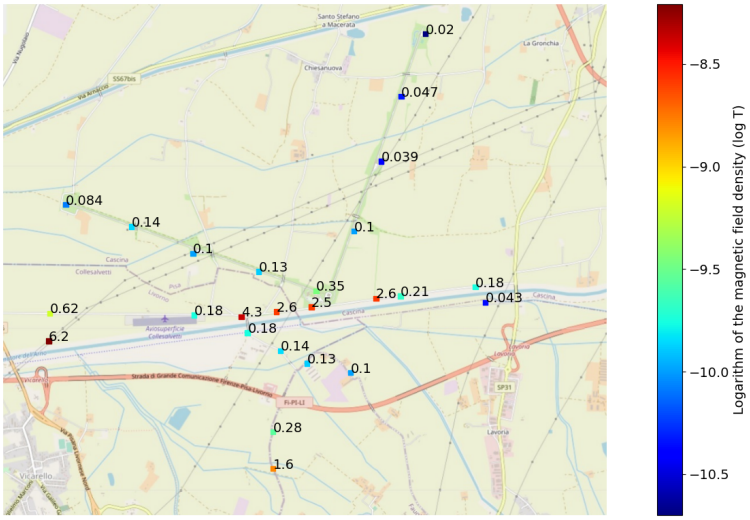

Figure 43: Map of the first magnetic survey

While going along the pipe, several metallic cages were found, around derivations of the pipes. The campaign was then made larger, with measurements in every direction to search for every potential source on a larger scale (in a 10km radius). By doing that series of measurements, three other pipelines were identified, from different companies.

This second survey lead us to discover a station located at the southwest of the Virgo entrance regrouping the different pipelines, indicated as "Gas pipe command center" on figure 44. We went to this station with an expert technician from the gas pipeline company who gave us useful information. A current is sent inside of these pipelines to prevent corrosion. This current is controlled at the central station. We went to that station and asked the technician to temporary switch off the current generator, and the signal identified by Virgo did not change.

We kept investigating, and performed a third series of measurements moving South-West from Virgo. We identified one more pipeline whose magnetic field was approximately 1000 times the one on the pipeline closer to Virgo. This pipe was then followed on the two ends: one end diminished to a little southern station, and the other was connected to a tinier control station a few kilometers east from the western central station, at which point the signal becomes null. This control station was found to have an isolating joint explaining the absence of signal on the other part.

Figure 44: Map of the noise hunt

We visited the small control station with the same company expert. Here another power generator was present. When switching it off the disturbance disappeared. The magnetic field seemed to be radiated from this pipe because of the current flow along the pipe. The company later agreed to change the settings of the alimentation for that pipeline. Its DC power supply was put in ”Constant Voltage” mode for unknown reasons during the days with external magnetometers off. Setting it again in ”Constant Current” mode solved the problem, removing the nuisance for the Virgo magnetometers, and a discussion to understand the reasons of that defectuous behaviour began after the end of the internship.

This noise shows an example of perturbation - a galvanic current of a few ampères inducting current inside of a pipeline that comes at $4000m$ of the Virgo interferometers - and the steps to identify the source, with another way to mitigate its effects, by setting the source to a less noisy, but still effective, operation mode.

References

[1] timothée Accadia et al. "The seismic Superattenuators of the Virgo gravitational waves interferometer". In: *J. Low Freq. Noise Vib. Act. Control* 30 (Jan. 2011), pp. 63–79.

[2] F Acernese et al. "Advanced Virgo: a second-generation interferometric gravitational wave detector". In: *Classical and Quantum Gravity* 32.2 (Dec. 2014), p. 024001. DOI: 10.1088/0264-9381/32/2/024001. URL: https://doi.org/10.1088%2F0264-9381%2F32%2F2%2F024001.

[3] Fausto Acernese et al. "The Advanced Virgo detector". In: *Journal of Physics: Conference Series* 610 (May 2015), p. 012014. DOI: 10.1088/1742-6596/610/1/012014.

[4] Irene Fiori et al. "The Hunt for Environmental Noise in Virgo during the Third Observing Run". In: *Galaxies* 8.4 (2020). ISSN: 2075-4434. DOI: 10.3390/galaxies8040082. URL: https://www.mdpi.com/2075-4434/8/4/82.

[5] Kamiel Janssens et al. "Impact of Schumann resonances on the Einstein Telescope and projections for the magnetic coupling function". In: (Oct. 2021).

[6] Alessandro Longo et al. "Scattered light noise characterisation at the Virgo interferometer with tvf-EMD adaptive algorithm". In: *Classical and Quantum Gravity* 37 (July 2020). DOI: 10.1088/1361-6382/ab9719.

[7] E A Mironov, A V Voitovich, and O V Palashov. "Permanent-magnet Faraday isolator with the field intensity of more than 3 tesla". In: *Laser Physics Letters* 17.1 (Nov. 2019), p. 015001. DOI: 10.1088/1612-202x/ab4fe3. URL: https://doi.org/10.1088/1612-202x/ab4fe3.

[8] Oleg V. Palashov et al. "High-vacuum-compatible high-power Faraday isolators for gravitational-wave interferometers". English. In: *Journal of the Optical Society of America B: Optical Physics* 29.7 (July 2012), pp. 1784–1792. ISSN: 0740-3224. DOI: 10.1364/JOSAB.29.001784.

[9] the Virgo Collaboration The LIGO Scientific Collaboration. "Observation of Gravitational Waves from a Binary Black Hole Merger". In: *Phys. Rev. Lett. 116* (2016). DOI: 10.1103/PhysRevLett.116.061102.